The Journal of Undergraduate Research in Physics

CONTENTS

Volume 13, Number 1
November, 1994

Published by the Physics Department of Guilford College
for
The American Institute of Physics and the Society of Physics Students

THE JOURNAL OF UNDERGRADUATE RESEARCH IN PHYSICS

This journal is devoted to research work done by undergraduate students in physics and its related fields. It is to be a vehicle for the exchange of ideas and information by undergraduate students. Information for students wishing to submit manuscripts for possible inclusion in the Journal follows.

ELIGIBILITY
The author(s) must have performed all work reported in the paper as an undergraduate student(s). The subject matter of the paper is open to any area of pure or applied physics or physics related field.

SPONSORSHIP
Each paper must be sponsored by a full-time faculty member of the department in which the research was done. A letter from the sponsor, certifying that the work was done by the author as an undergraduate and that the sponsor is willing to be acknowledged at the end of the paper, must accompany the manuscript if it is to be considered for publication.

SUBMISSION
Two copies of the manuscript, the letter from the sponsor and a telephone number or E-Mail address where the author can be reached should be sent to:

Dr. Rexford E. Adelberger, Editor
THE JOURNAL OF UNDERGRADUATE
RESEARCH IN PHYSICS
Physics Department
Guilford College
Greensboro, NC 27410

FORM
The manuscript should be typed, double spaced, on 8 1/2 x 11 inch sheets. Margins of about 1.5 inches should be left on the top, sides, and bottom of each page. Papers should be limited to fifteen pages of text in addition to an abstract (not to exceed 250 words) and appropriate drawings, pictures, and tables.

Manuscripts may be submitted on a disk that can be read by a MacIntosh™. The files must be compatible with MacWrite™, MicroSoft Word™ , PageMaker™ or WordPerfect™.

ILLUSTRATIONS
Line drawings should be made with black ink on plain white paper. Each figure or table must be on a separate sheet. Photographs must have a high gloss finish. If the submission is on a disk, the illustrations should be in PICT, TIFF or EPS format.

CAPTIONS
A brief caption should be provided for each illustration or table, but it should not be part of the figure. The captions should be listed together at the end of the manuscript

EQUATIONS
Equations should appear on separate lines, and may be written in black ink. We use EXPRESSIONIST™ to format equations in the Journal.

FOOTNOTES
Footnotes should be typed, double spaced and grouped together in sequence at the end of the manuscript.

PREPARING A MANUSCRIPT
A more detailed set of instructions for authors wishing to prepare manuscripts for publication in the Journal of Undergraduate Research in Physics can be found in Volume 8 #1 which appeared in October of 1989 or in Volume 11 #2 which appeared in May of 1993.

SUBSCRIPTION INFORMATION

The Journal is published twice each academic year, issue # 1 appearing in November and issue # 2 in May of the next year. There are two issues per volume.

TYPE OF SUBSCRIBER	PRICE PER VOLUME
Individual	$US 5.00
Institution	$US 10.00

Foreign subscribers add $US 2.00 for surface postage, $US 10.00 for air freight.

Back issues may be purchased by sending $US 15.00 per volume to the editorial office.

To receive a subscription, send your name, address, and check made out to **The Journal of Undergraduate Research in Physics (JURP)** to the editorial office:

JURP
Physics Department
Guilford College
Greensboro, NC 27410

The Journal of Undergraduate Research in Physics is sent to each member of the Society of Physics Students as part of their annual dues.

VOLUME 13

ACADEMIC YEAR 1994-1995

The Journal of Undergraduate Research in Physics

ISSN 0731 - 3764

Published by the Physics Department
of Guilford College
for
The American Institute of Physics
and
The Society of Physics Students

STUDY OF THE RESONANCE OF A LOW-FREQUENCY SPEAKER USING LASER DOPPLER VELOCIMETRY

Todd E. Wiest* and Timothy R. Cerniglia**
Physics Department
Wilkes University
Wilkes-Barre, PA 18766
received April 6, 1993

ABSTRACT

The oscillations of a low-frequency speaker (woofer) were studied to determine its motion at different driving frequencies. Laser Doppler Velocimetry techniques were employed in conjunction with a Michelson Interferometer. The linearity of the oscillations was studied. The amplitudes of these oscillations as a function of the frequency driving the speaker were compared to a theoretical resonance curve.

INTRODUCTION

Laser Doppler Velocimetry (LDV) is an application of the Doppler effect. The Doppler effect involves two physical phenomena. One of these is the modulation of the amplitude of two signals when they are superimposed. This amplitude modulation creates a beat pattern with a frequency independent of the frequencies of the two signals ν and ν_o, but dependent on the difference of the two frequencies $\Delta\nu$:

$$\Delta\nu = \nu - \nu o \,, \tag{1}$$

When one of the sources of these signals is in motion relative to the other source of known frequency, the frequency of the moving signal is: [1]

$$\nu = \nu_o \sqrt{\frac{1-\frac{v}{c}}{1+\frac{v}{c}}} \,, \tag{2}$$

where v is the velocity of the source and c is the speed of light. When the beat frequency is also known, solving Equation 1 for νo gives the relative velocities between the two sources as:

$$\nu + c\left(\frac{1-\frac{v^2}{v_o^2}}{1+\frac{v^2}{v_o^2}}\right) \tag{3}$$

By employing a laser as a source of the signal, the frequency of the source signal is well determined.

When this laser is used as the source for a Michelson interferometer, two light beams are produced that are of the same frequency. When the light in one of the arms is incident on a moving object, the frequency of that light is changed due to the Doppler effect. When this light is recombined with the light from the other arm of the

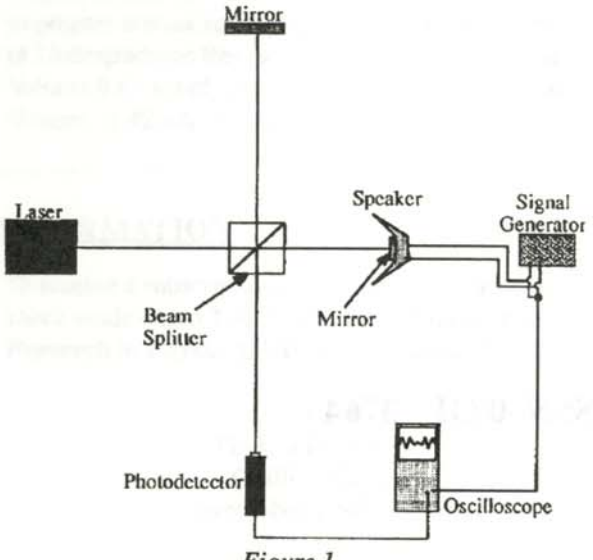

Figure 1
Michelson interferometer configuration with the test arm containing a mirror attached to a low frequency speaker.

Both authors graduated from Wilkes University, Tim in 1992 and Todd in 1993, and entered the air force. Todd is presently working on his M.Sc. at the Air Force Institute of Technology. He is currently researching nitrosyl bromide to determine the rotational parameters of the NO bond stretch (0 to 2 vibrational levels) transition. Upon completion of the degree in December, he will be reassigned to Rome Laboratory, Griffiss AFB, Rome, New York. Tim is stationed Colorado where he is working in the Milstar space satellite operations.

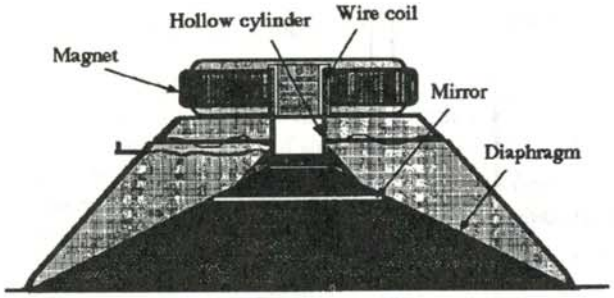

Figure 2

Diagram of the moving coil speaker used in this experiment. The wire coil oscillates in the magnetic field to move the diaphragm.

interferometer, the standard interference pattern is seen, but the amplitude of this pattern is modulated.

MICHELSON INTERFEROMETER THEORY

In a Michelson interferometer, such as shown in Figure 1, the intensity I of the light at the detector is given by [2]:

$$I = I_1 + I_2 + 2\sqrt{I_1 I_2}\cos\left(\frac{4\pi d}{\lambda_o}\right) \qquad (4)$$

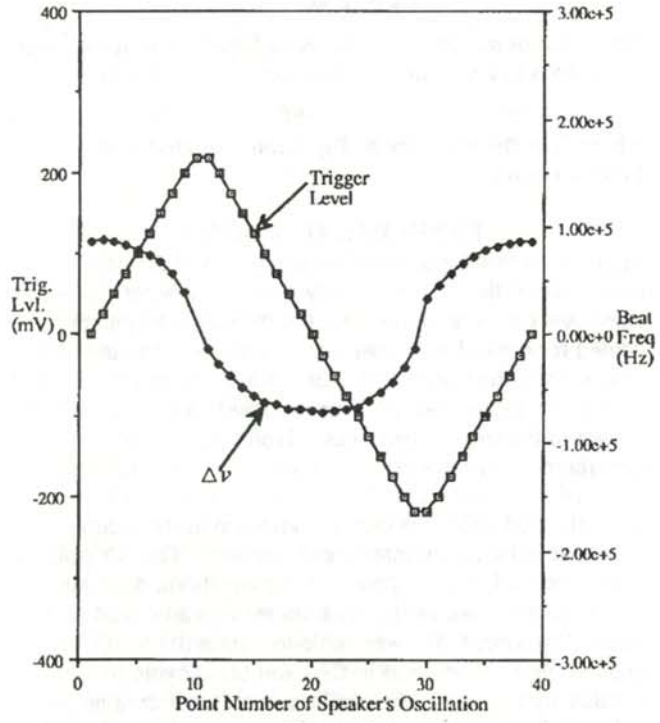

Figure 3

Beat frequency versus the phase (triggering level) of the voltage function that was driving the speaker at 60 Hz. The horizontal scale is the point on the speaker's drive signal. The sinusoidal variation of the frequency shows that the speaker was operating in its linear response region.

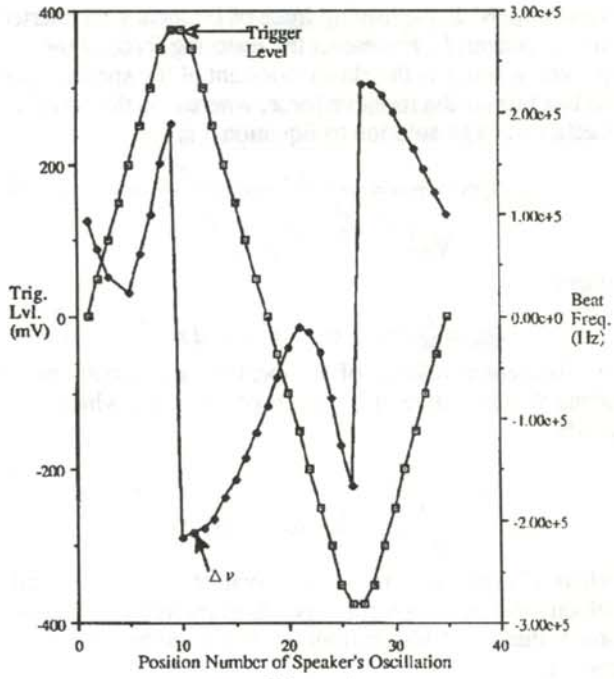

Figure 4

Beat frequency versus position for the speaker cone at a driving frequency of 40 Hz. The horizontal axis the point on the speaker's drive signal. The non-sinusoidal response indicated that the speaker was being operated in its non-linear region.

where I_1 is the intensity of the reference beam, I_2 is the intensity of the test beam, and d is the optical path difference between the two arms of the interferometer. The third term in Equation 4 is the interference term. When one of the mirrors of the interferometer is attached to a speaker that is being driven at some frequency, the distance d in Equation 4 changes sinusoidally with the speaker motion. As a result, the amplitude of the interference term changes with time. The frequency at which the interference terms changes is the so-called beat frequency.

Viewing the speaker as the "source" of the light in the test arm of the interferometer and the fixed mirror as the "source" of in the reference arm, one can measure the velocity of the speaker using the Doppler effect. With the beat frequency obtained from the amplitude modulation of the interference pattern and the known frequency of the light in the reference arm, Equation 3 can be used to find the velocity of the speaker.

THEORETICAL MOTION OF SPEAKER

The equation of motion of the speaker was obtained by considering the forces acting on the system [4]

$$m\frac{d^2\xi}{dt^2} = I_o e^{i\omega_1 t} - \kappa\,\xi - r_e\frac{d\xi}{dt}, \qquad (5)$$

where m is the mass of the diaphragm, coil and mirror; ξ is the distance moved by the speaker (related to d in Equa-

tion 4); $I_o e^{i\omega_1 t}$ is the driving force of frequency ω_1 exerted on the speaker; $k\xi$ represents the restoring force of the speaker, where k is the elastic constant of the speaker; and the last term is the resistive force, where r_e is the resistive coefficient. The solution to Equation 5 is [4]

$$\xi = \frac{a_o}{\sqrt{\left(\omega_o^2 - \frac{r^2}{2} - \omega_1^2\right)^2 + \omega_o^2 r^2 - \frac{r^4}{4}}}, \qquad (6)$$

where

$$a_o = \frac{I_o}{m} e^{i\omega_1 t}, \quad \omega_o = \sqrt{\frac{K}{m}} \text{ and } r = \frac{r_e}{m}. \qquad (7)$$

The theoretical velocity of the speaker can be found by taking the derivative of ξ with respect to time, which yields:

$$v = \frac{a_o \omega}{\sqrt{\left(\omega_o^2 - \frac{r^2}{2} - \omega_1^2\right)^2 + \omega_o^2 r^2 - \frac{r^4}{4}}} \qquad (8)$$

Where v is the real part of the derivative. The theoretical velocity in Equation 8 corresponds to the velocity (Equation 3) that is calculated from the measured beat frequency.

When driven at the resonance frequency, ω_R, the first term of the denominator in Equation 6 is equal to zero. From this we find that:

$$\omega_R = \sqrt{\omega_o^2 - \frac{r^2}{2}} \qquad (9)$$

The value of a_o can be found using Equation 6 in the limit as ω_1 goes to zero. In this case, Equation 6 becomes:

$$a_o = \xi_o \omega_o^2 \qquad (10)$$

where ξ_o is the intercept of Equation 3 plotted as a function of ω_1.

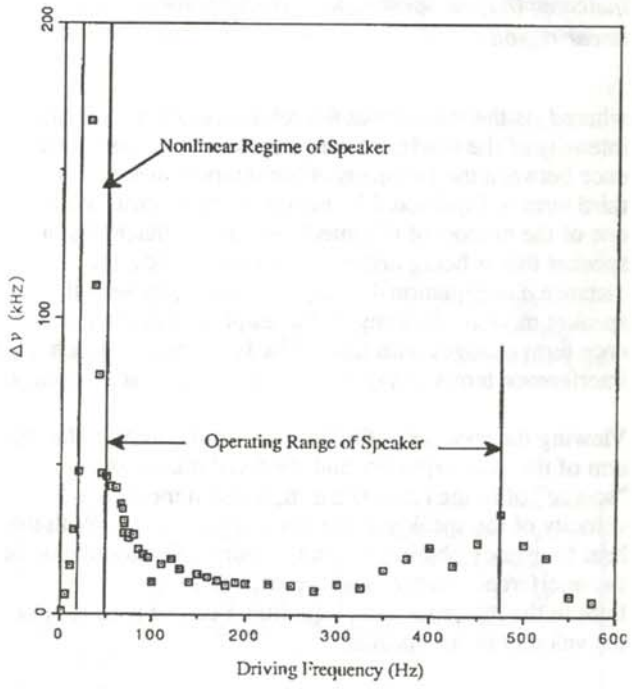

Figure 5

Beat frequency as a function of the driving frequency applied to the low-frequency speaker. The trigger level was set at 0V. The region where the beat frequency is high is where the speaker exhibits non-linear behavior. correspond to high velocities of the speaker. This is the non-linear region of the speaker.

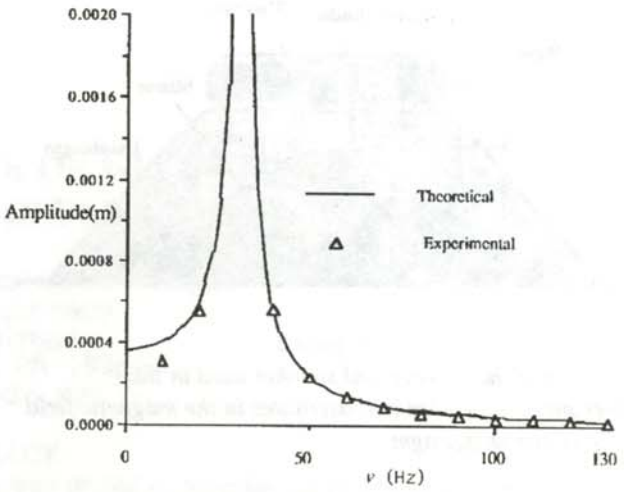

Figure 6

Amplitude of the motion of the low-frequency speaker as a function of the frequency of the driving voltage. The triangles are the data and the solid line is the results using Equation 6.

EXPERIMENTAL SETUP

Figure 1 shows the experimental setup used to study the resonance of the low-frequency speaker (woofer). A HeNe laser (λ = 632.8 nm) was directed through a beam splitter coated for optical wavelengths between 400 nm and 700 nm. One of the beams reflected off a stationary mirror and the other reflected off a mirror mounted on the speaker, as shown in Figure 2, which was driven by a function generator. [3] The reflecting surface of each mirror was made of titanium oxide (TiO_2) with a reflectivity Γ = .588. The reflected light was then recombined at the beam splitter to produce an interference pattern. The 'Doppler beat frequencies' were detected with a silicon detector. The voltage output of the photometer was analyzed with an oscilloscope. [4] We were able to obtain the beat frequency for each position in the oscillation cycle of the speaker by triggering the oscilloscope at different amplitudes of the signal that was driving the speaker. The trace of the interferometer signal as viewed on the oscilloscope was a sinusoid with modulated amplitude. By finding a complete cycle of the modulating amplitude, the beat frequency could be ye points with the oscilloscope's built-in time markers. The difference between these two marks was calculated by the oscilloscope and the inverse of this

value calculated to obtain the beat frequency.

EXPERIMENTAL RESULTS

Figure 3 shows a plot of the data taken with a drive signal of 60Hz at various phases of the voltage function driving the speaker. Each different beat frequency corresponds to a different location of the motion of the speaker. The coherent relationship (both appear to be sinusoidal functions with the same period) between the motion of the speaker and the driving function indicate that the speaker is behaving in a linear fashion. 60 Hz is in the operating range of the speaker.

Figure 4 shows a quite different situation. The beat frequency does not have the same shape as the driving function, so there is a non linearity of the motion of the speaker at this frequency.

Figure 5 is a plot of the beat frequencies found with the trigger of the oscilloscope set at the 0.0V level as a function of the driving frequency. Notice that in the region from 15Hz to 50Hz, the beat frequency is very much higher than for the rest of the drive frequencies. These high values for the beat frequency

At resonance, the amplitude of the oscillations becomes very large. When this occurs, the velocity of the oscillatory must also increase and the oscillator becomes nonlinear because the amplitude has grown exponentially.

The theory for the motion of the moving-coil speaker, Equation 8, allows us to convert the beat frequencies to velocity and then to amplitude to compare theoretical and experimental curves. An arithmetic mean velocity of the calculated velocities was found for each drive frequency. The velocity was then divided by the angular frequency of the drive signal to determine the average displacement of the speaker for that drive frequency. Equations 9 and 10 were used to find the values of the parameters a_o, ω_o and r to use in Equation 6. Figure 6 shows the results of the experimental amplitude data and the results predicted by Equation 6. This graph indicated that the theoretical model agrees quite well with the experimental results.

ACKNOWLEDGMENTS

The authors would like to thank Dr. Yu Wang Bibby for her efforts in acquiring optical components for our research. We also thank Dr. Hong Yuan Ling for his help in refining the theory for the moving coil forced oscillation and his thoughtful guidance and encouragement. We also greatly appreciate David Moss for his help with the thin film processing.

REFERENCES

1. Robert D. Guenther, Modern Optics, J. Wiley & Sons, New York, 1990.
2. *Ibid.*
3. Hewlett Packard 8904A Multifunction Synthesizer.
4. N.W. McLachlan, Loud Speakers, Oxford University Press, New York, 1934.
5. Hewlett Packard 54503A Digitizing Oscilloscope.

FACULTY SPONSOR

Dr. Roger Maxwell
Department of Physics
Chairman, School of Science and Engineering
Wilkes University
Wilkes-Barre, PA 18766-0001

* current address of author : 5867 Troy Villa Blvd., Huber Heights, OH 45424-2649.
** current address of author : 4th Space Operation Squadron, 300 O'Malley Avenue, Suite 53, Falcon AFB, Colorado Springs, CO 80912.

PRODUCTION OF C_{60} AND C_{70} MOLECULES

Michael S. Cox *, Kenneth Peek° and Shane Denton§
Department of Physics
Texas Tech University
Lubbock, TX 79409-1051
received June 2, 1993

ABSTRACT

Synthesis of the C_{60} and C_{70} Buckminsterfullerenes was achieved through the arc-vaporization of graphite rods. The carbon was vaporized using a high current DC plasma arc in an inert helium atmosphere. A Pyrex bell jar was initially evacuated to approximately 10^{-6} Torr and then backfilled to 50-200 Torr with helium. The arc was stable when the rods had a separation of 1.2 mm. Fullerene yields for burn times up to 2.5 hours varied from less than 1% to as much as 3% of the residual soot collected. The C_{60} and C_{70} were separated from the soot by soxhlet extraction. The resulting benzene/fullerene solution was purified through the use of column chromatography. A C^{13} NMR study of the purified sample confirmed the presence of the "buckyballs"

INTRODUCTION

The discovery of the heavy carbon molecules, the C60 and C_{70} "fullerenes" by Smalley and Kroto *et.al.* [1] has generated an entirely new field of study, "buckyball science", named for the architect Buckminster Fuller. Geodesic domes, for which he is famous, resemble the structure of the C_{60} and C_{70} molecules. Discovery of a high efficiency method of producing the molecules has made research into buckyballs practical.[2] Interest has been fueled by projected applications ranging from diamond semiconductor growth substrate to a new reaction mass for ion engines.

The focus of this research has been on the C_{60} molecule. This molecule is a soccer ball shaped object, that is, it has the shape of a truncated icosahedron, consisting of hexagonal and pentagonal facets composed of carbon atoms in ring form (see Figure 1). The molecule is the first entirely pure form of carbon. Because it has a closed molecular shape, and has shown a reluctance to form compounds, it does not carry surface contaminants as diamond and graphite naturally do.

The process of formation is still not well understood, but the method of production and optimal conditions for fullerene production have been defined. Our experiment was devoted to the synthesis of fullerene molecules under these optimal conditions and to the construction of an efficient low cost C_{60} generator.

OPTIMAL FORMATION CONDITIONS

Synthesis of C_{60} and C_{70} is achieved using high current arc-vaporization of graphite rods in an inert helium atmosphere. The optimum conditions for fullerene production are still debated in terms of exact arc type, temperatures and quenching gas pressures. The basic requirements for these parameters, however, are well enough established that

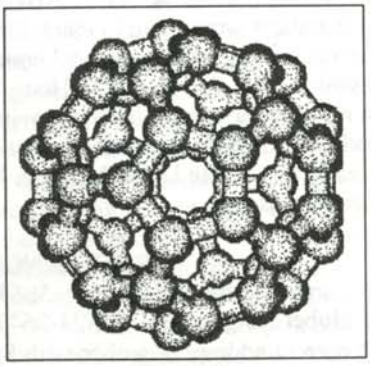

Figure 1
Geometry of C_{60} "buckminsterfullerene"

Mike Cox graduated in May, 1994 with a B.S. in physics from Texas Tech University, where he is pursuing a graduate degree in physics. Ken Peek will receive his B.S. in engineering physics from Texas Tech University in December of 1994. Shane Denton graduated in May, 1994 with a B.S. in engineering physics from Texas Tech University, where he is pursuing a graduate degree in Engineering.

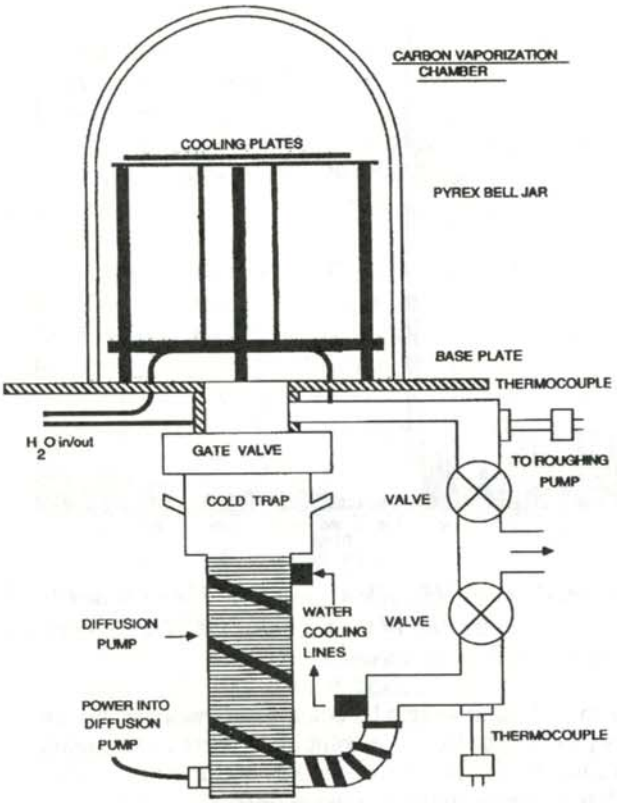

Figure 2
Schematic diagram of the carbon vaporization chamber.

anyone can make fullerenes as long as they observe the following constraints.

Arc type generators [3,4] may use either alternating current or direct current, but the current must be maintained between 50 A to 100 A, while keeping the voltage high enough to maintain the arc, typically between 15V and 50 V. Many laboratory power supplies are suitable for this task, but arc welding power supplies (even common household welders) have been used successfully. We found that a 2kW metal evaporator transformer was adequate for a low power arc.

The temperature of the carbon vaporized in the arc ranges from over 3620C to the temperature of the chamber wall, usually slightly warmer than room temperature. Between these extremes, there exists a zone around the arc where the temperature hovers at approximately 1200C. This is the temperature region that is the most conducive to fullerene formation.[5]

The temperature is directly affected by the pressure of the quenching gas. The quenching gas is usually helium at a pressure between 50 Torr and 400 Torr. The most common pressures for high recovery rates are 100 Torr to 200 Torr. The gas absorbs kinetic energy from the highly ionized carbon gas leaving the arc, cooling it some distance from the arc. The higher pressure allows the carbon to cool while it is closer to the arc, while the carbon is still fairly dense. Under these conditions, C_{70} molecules form in greater abundance than at 100 Torr, where they are rare. At lower pressure, the fullerenes form in a less dense gas of ionized carbon, and thus the smaller C_{60} molecules comprise almost all of the fullerenes produced. (Heavier fullerenes are produced in decreasing abundance and in even number of atoms, i.e. C_{70}, C_{76}, C_{78}, C_{84}, etc.)

APPARATUS

Bell Jar

Our apparatus consisted of a standard bell-jar vacuum chamber with an oil diffusion pump as schematically shown in Figure 2. We used a large mechanical pump to achieve a rough evacuation of the chamber and then to pump the high side of the diffusion pump. The liquid nitrogen cold trap was used to prevent oil backstreaming into the evacuated chamber.

Main Power Circuit

A schematic of the power circuit is shown in Figure 3. We obtained a 2kW 220 VAC single phase transformer (20V,100A output) from a metal evaporation system. The input voltage was regulated with a 220V Variac variable transformer. We constructed a rectifier circuit with diodes capable of handling up to 600A spikes at 400V. The rectified output was routed through a 195μH inductor to prevent current spikes from overloading the diodes. The output was routed to high current feedthroughs into the vacuum chamber, and then by fiberglass insulated braided copper cables to the carbon rods to produce the carbon arc.

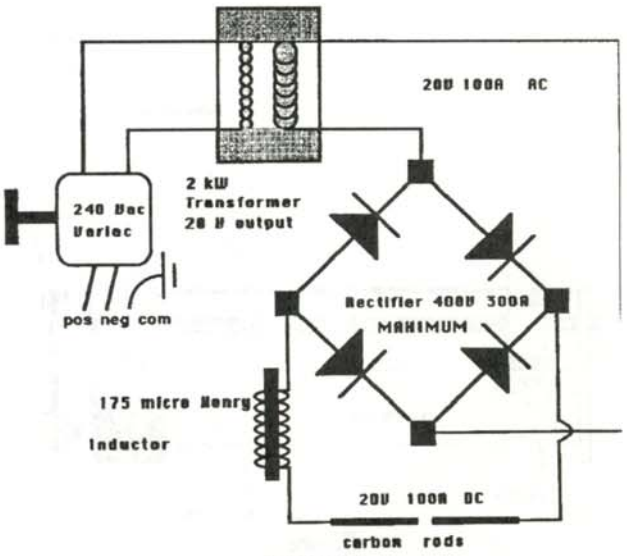

Figure 3
Schematic diagram of the main power circuit.

Carbon Rod Manipulator

The apparatus for the gap adjustment of the carbon arc was constructed from an aluminum air track with two aluminium gliders connected by a screw drive mechanism as shown in Figure 4. The screw drive was actuated by a 120VAC 9 rpm reversible motor, which was controlled manually from outside the chamber. The manipulator was placed between two copper plates which were continuously fed cooling water from a 160 psi source line.

Operation of the Carbon Arc

The chamber was pumped down to approximately 20 microns (10^{-6} Torr) with the combination of mechanical and nitrogen cooled diffusion pumps. At this time, the chamber was backfilled to approximately 200 Torr with helium gas. The main power circuit was energized with the rods 4 cm-5 cm apart. The rods were moved together until they touched, and the arc began. The separation of the rods was adjusted for maximum brightness and allowed to continue. The optimum separation was approximately 1 mm at full power. A great deal of "soot" then accumulated on all the exposed surfaces in the chamber.

Collection and Purification of the "Soot"

The soot generated in the "burning" of these rods was collected using microscope slides scrape the interior surfaces. The elemental carbon/fullerene mixture was then purified through soxhlet extraction in solution with benzene, toluene or similar organic solvents.

Soxhlet extraction is a process in which the "soot" is placed in a container of heated solvent. This dissolved fullerenes pass out of the container in the vapor stage of the solvent. The vapor is then condensed on a cold finger and the resulting concentrated solution is collected in a separate container. This mixture is then separated according to molecular weight by column chromatography. In this process, the fullerene solution is poured into a glass column of silica power. Molecules of differing weights will travel through the column at different speeds, allowing the molecules of like mass to be washed out with addition of more solvent. The resulting solutions man then be rid of solvent by evaporation under a hood.

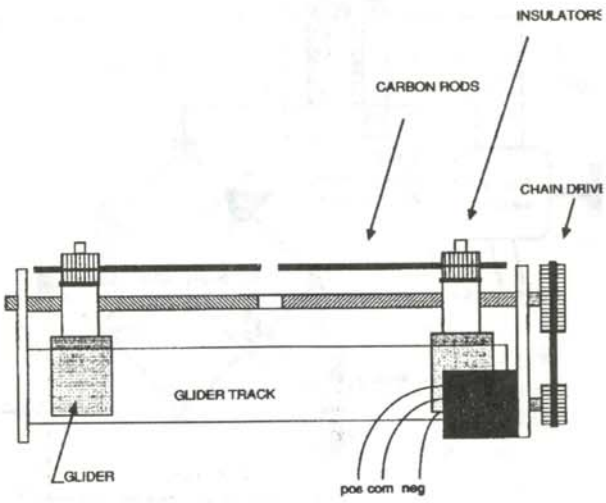

Figure 4

Schematic representation of the manipulator for the vaporizing rods.

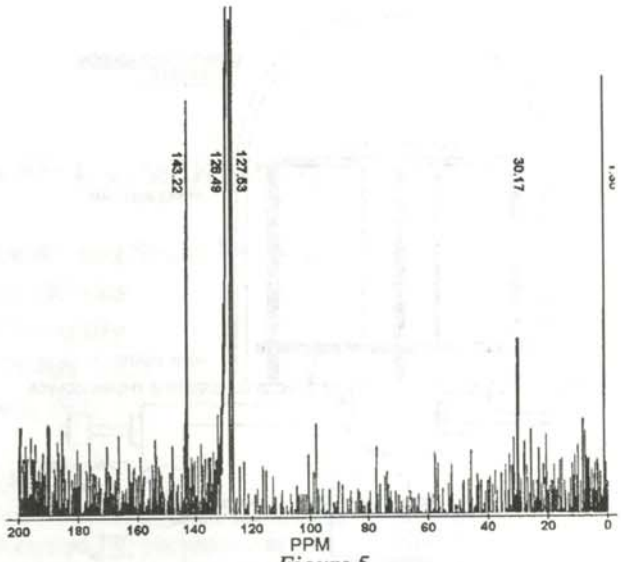

Figure 5

The results of the 13C NMR spectrum. The peak at 143.22 ppm is representative of the C_{60} molecule. The other peaks are from the organic solvents.

We achieved a recovery of about 3% fullerenes as compared to the weight of the collected soot. We produced both C_{60} and C_{70} , as well as other fullerenes that were left as residue in amounts too small to be effectively separated. The presence of C_{60} was confirmed by ^{13}C NMR. The spectrum is shown in Figure 5. The peaks at 1.35 ppm and 30.17 ppm are indicative of the hexane solvent. The triplet peak between 127.53ppm and 128.49 ppm is indicative of the benzene solvent. The final peak at 153.22 ppm indicates the presence of the C_{60} molecule. This matched the results of other NMR studies of C_{60} .[7] An ionization mass spectrum of the C_{60}/C_{70} mixture revealed the presence of fragments of the buckyballs, but destroyed the buckyballs in the ionization process, such that no large masses were found intact.

ACKNOWLEDGMENTS

This work would not have been possible without the help and support of the following people: Dr. David Lamp, Dr. Pete Seibt, Dr. Randall Peters, Dr. David Birney, Bob Birch, Richard Hernandez and William Stubbs.

REFERENCES

* Present address : Physics Department, Texas Tech University, Lubbock, TX 79409-1051, tlmsc@ttacs3.ttu.edu.
° Present address: Department of Physics, Texas Tech University, Lubbock, TX 79409-1051.
§ Present address: Texas Tech University, Lubbock TX 79409.

1. H.W. Kroto, J.R. Heath, S.C. O'Brien, R.F. Curl, R.F. Smalley, Nature, 318, (1985), p. 162.
2. W. Krätschmer, L.D. Lamb, K, Fostiropoulos, D.R. Huffman, Nature, 347, (1990), p. 354.
3. D.H. Parker, P. Wurz, K. Chatterjee, K.R. Lykke, J.E. Hunt, M.J. Pellin, J.C. Hemminger, D.M. Gruen, L.M. Stock, J. Am. Chem. Soc., 113, (1991), p. 7499.
4. R.E. Haufler, J. Conceicao, L.P.F. Chibante, Y, Chai, N.E. Byrne, S. Flanagan, M.M. Haley, S.C. O'Brien, C. Pan, Z. Xiao, W.E. Billups, M.A. Ciufolini, R.H. Hauge, J.L. Margave, L.J. Wilson, R.F. Curl, R.E. Smalley, J. Phys. Chem., 94, (1990), p. 8634.
5. R.E. Smalley, "Doping the Fullerenes", TTU Department of Physics Colloquium Series, March 1992, Texas Tech University, Lubbock, TX.
6. R. Malhotra, D.S. Ross, J. Phys. Chem., 95, (1991) p. 4599.
7. H.W. Kroto, A.W. Allaf, S.P. Balm, Chem. Rev., 91, (1991), P. 1213.

FACULTY SPONSOR

Dr. C. David Lamp
Department of Physics
Texas Tech University
Lubbock, TX 79409-1051

A STUDY OF THE FEASIBILITY OF PERFORMING AN η' PHOTOPRODUCTION EXPERIMENT AT CEBAF

Brian M. McKeever
Department of Physics
University of Richmond
Richmond, VA 23173
received August 4, 1994

ABSTRACT

In light of the failure of the quark model to predict accurately the mass of the η' meson, the question of the structure of the η' has attracted considerable interest. As part of the preliminary work on this problem, we have performed a study to evaluate the feasibility of using the Continuous Electron Beam Accelerator Facility (CEBAF) and the CEBAF Large Acceptance Spectrometer (CLAS) to measure the photoproduction of η' mesons in nuclei. The results of such an experiment would be used to obtain information on the η' -nucleon interaction, which in turn would provide an insight into the structure of the η'. The computer simulations yielded reasonable detection efficiencies (>12%) and good particle identification, indicating that the experiment is quite feasible.

BACKGROUND

The quark model has been very successful in predicting the spectra of strongly interacting particles. However, there is a significant discrepancy between the observed mass for the η' meson and the mass predicted by simple relationships between the mesons based on the quark model. [1,2] It has been suggested that this is the result of the η' being something other than the quark-antiquark pair as assumed in the quark model. Perhaps it has a significant gluonic component in addition to the two quarks. [1,3] By measuring the photoproduction of η' mesons on nuclear targets, and comparing this with similar measurements [2] taken on a hydrogen target, we can obtain information of the η' -nucleon interaction and about the structure of the η'.

CEBAF

The Continuous Electron Beam Accelerator Facility (CEBAF), currently under construction in Newport News, Virginia, is a superconducting electron accelerator that will be capable of producing a beam of electrons with energies as high as 4 GeV. The beam can be sent to the three experimental halls simultaneously. Hall B has instrumentation that is well suited for photoproduction experiments.

Brian is a junior physics/math major at the University of Richmond. This research was done the summer following his freshman year and was presented the following spring at the National Conference on Undergraduate Research. Brian's future plans include graduate school, where he will most likely study math.

It is equipped with a Bremsstrahlung photon tagging system. This system consists of a radiator, used to decelerate the incoming electrons, causing them to radiate a photon. Most of the electrons make it through the radiator unaffected. If the Bremsstrahlung system causes an electron to radiate a photon, the remaining energy of the electron is measured, allowing the energy of the incident photon to be tagged. This 'tagged' photon will be used in our photoproduction experiment. The CEBAF beam's duty factor is essentially continuous wave, so there is a very low accidental coincidence rate, leading to a reduced background noise.

Most importantly, Hall B contains the CEBAF Large Acceptance Spectrometer (CLAS), which is almost a "4π" detector. This feature makes it possible to perform an experiment that requires the analysis of a number of particles in the final state. CLAS, shown in Figure 1, comprises six separate sections, each subtending a ϕ angle of 60°. The sectors are separated by six superconducting coils which produced a nearly toroidal magnetic field. The toroidal magnet field bends charged particles, aiding in particle identification. The spaces between these coils are shaped somewhat like orange sections and house the detector packages.

Figure 2 shows the different components that make up CLAS. Each sector contains three regions of drift chambers, Cerenkov counters, scintillation counters and shower calorimeters. The drift chambers will be used to determine the trajectories of charged particles. The Cerenkov counters will be used to discriminate between electrons and other negatively charged particles (such as the π-) The scintillation counters will be used to trigger the detector and to perform time-of-flight measurements. The electro-

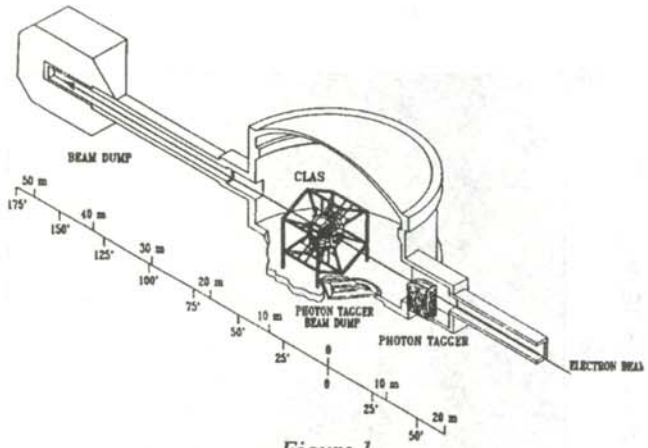

Figure 1

A perspective view of the interior of CEBAF Hall B, showing the CLAS, the photon tagging system and the beam dump. The beam enteres from the right.

magnetic shower calorimeter will be used for detecting and discriminating between photons and neutrons as well at detecting electrons.

For our simulations, we made the following assumptions about detector coverage:

° the drift chambers and scintillation counters cover polar angles from 8° to 140°

° the Cerenkov counters cover the forward 45°

° the shower calorimeters cover the forward 45° in four of the six sectors, but are extended out to 75° in the two opposite sectors.

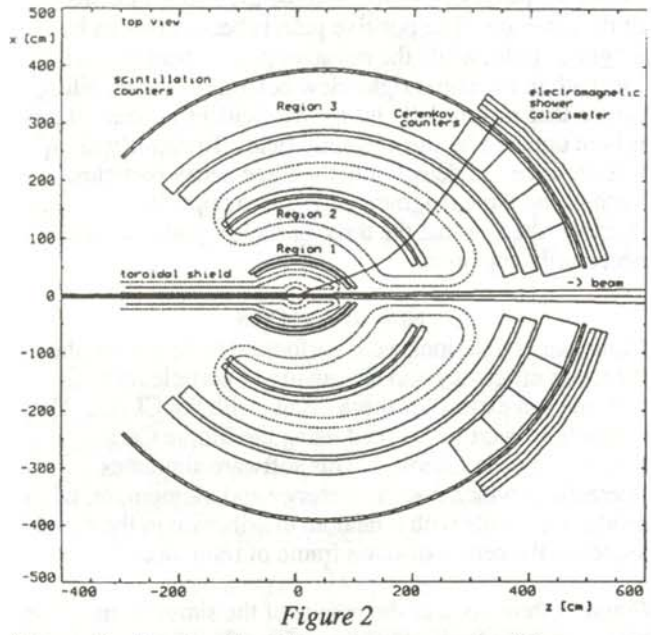

Figure 2

Schematic showing the different components of the detectors in CEBAF Hall B and their respective sizes. The areas labelled Regions 1,2 and 3 are the three drift chambers. The path shown is that of a particle with momentum 1 GeV/c.

EXPERIMENTAL APPROACH

The lifetime of the η' is so short a traditional scattering experiment where a beam of them is incident on a target. A beam of η''s would decay before they could reach a target. For this reason, they must be produced inside the nuclei of the target material. In our approach, we use an electron beam of energy of 2.4 GeV to produce a beam of photons with energies below the photoproduction threshold energy (1.466 Gev on a single proton, but lower in the nucleus due to the Fermi motion of the nucleons) to approximately 2.25 GeV. This will provide sufficient energy to photoproduce an η' meson on a nucleon inside the nucleus. The η' then has the opportunity to interact with the other nucleons in the nucleus as it propagates through it. In essence, by creating the η' inside the nucleus, we are using the nucleus as a laboratory. If the η' meson is not absorbed by one of the other nucleons in the nucleus, its lifetime allow it sufficient time to exit the nucleus before it decays.

Figure 3 shows what might happen inside the nucleus during a typical event. The incident photon strikes a nucleon in the target material, photoproducing an η' meson. This η' may then collide with another nucleon before making its way out of the nucleus, where it then decays. Another possibility is that instead of scattering off the nucleon, the η' meson is absorbed. By photoproducing the η' on a variety of nuclear targets, we will be able to determine the target dependence of the production cross section per nucleon. If we compare this with the cross section data from a proton (hydrogen nucleus) target, we will be able to extract information on the η' -nucleon interaction.

DECAY MODE

The η' has three common decay modes:

$$\eta' \rightarrow \pi^+ + \pi^- + \eta$$
$$\eta' \rightarrow \pi^o + \gamma$$
$$\eta' \rightarrow \pi^o + \pi^o + \eta\,,$$

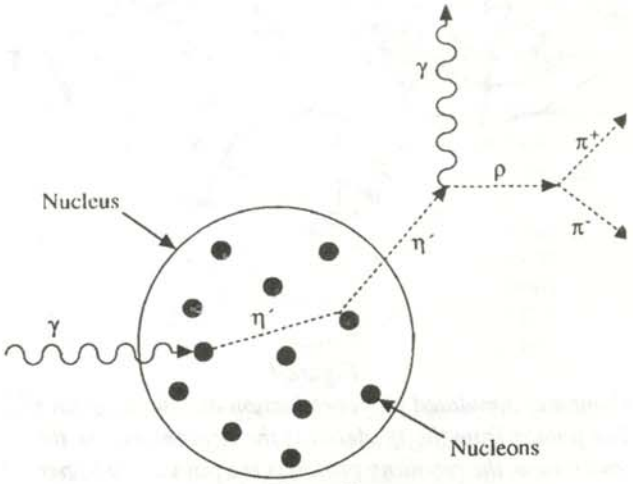

Figure 3

An example of an η' being photoproduced inside a nucleus.

with branching ratios of 44.1%, 30.0% and 20.6% respectively.[4] In this study, we will detect the η' via the $\rho\gamma$ decay, where the ρ meson in turn decays into a π^+ and π^-. There are three basic reasons for choosing to look for this decay mode as opposed to the others, The first is that it has a reasonably large branching ratio. The second is that it has a high detection rate, due to the fact that there are only three final decay particles. Since the meson decays most often into either $\gamma\gamma$, $\pi^o\pi^o\pi^o$ or $\pi^+\pi^-\pi^o$, and the π^o decays into $\gamma\gamma$, the other two most common decay modes each produce a minimum of four particles, each of which must be detected to identify the η' . Finally, in the $\eta' \rightarrow \pi^o + \gamma$ decay mode, a majority of the particles produced are charged, which the CEBAF instruments can detect over a larger solid angle and with a higher degree of accuracy than neutral ones.

CLAS will be used to identify the reaction products and to determine their energies and production angles in the laboratory frame of reference. From this information, their four-momentum vectors can be calculated. Using Equation 1,

$$E^2 = (cp)^2 + (mc^2)^2 \qquad (1)$$

which relates rest mass, energy and momentum, we determine the mass and four-momentum vector of the particle that must have produced them.

$$M_{\eta'}^2 = (E_{\pi^+}^2 + E_{\pi^-}^2 + E_\gamma^2)^2 / c^4 + (\vec{p}_{\pi^+} + \vec{p}_{\pi^-} + \vec{p}_\gamma)^2 \qquad (2)$$

Figure 4 shows the result of a computer simulated event in which all three particles strike the necessary detectors. The incident photon enters from the left and strikes the target in the middle of the diagram. The straight line in the lower view is the path of the photon that results from the η' decay. Since it is a neutral particle, it is unaffected by the magnetic field that bends the other particles, it goes straight out to the shower calorimeter. The upper left view shows the paths of the two charged pions from the decay of the ρ meson. The positive pion is bent outwards by the magnetic field, while the negative pion is bent inward. The path in the upper right view belongs to the recoiling proton that was initially hit by the incident photon. It too is bent outward by the magnetic field. To identify the η', it is necessary to detect only the three decay particles. Each of the three diagrams shows two opposing sectors, to illustrate the fact that the three particles' paths are not necessarily coplanar.

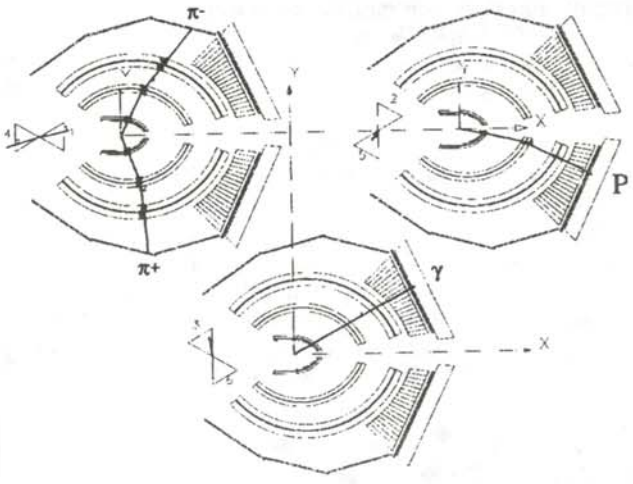

Figure 4

Computer simulated photoproduction and decay of an η'. The photon from the η' decay is the straight path in the lower view, the recoiling proton is the path in the upper right view, and the two pions are the particles in the upper left view. The positive pion is bent outward by the magnetic field, while the negative pion is bent inward.

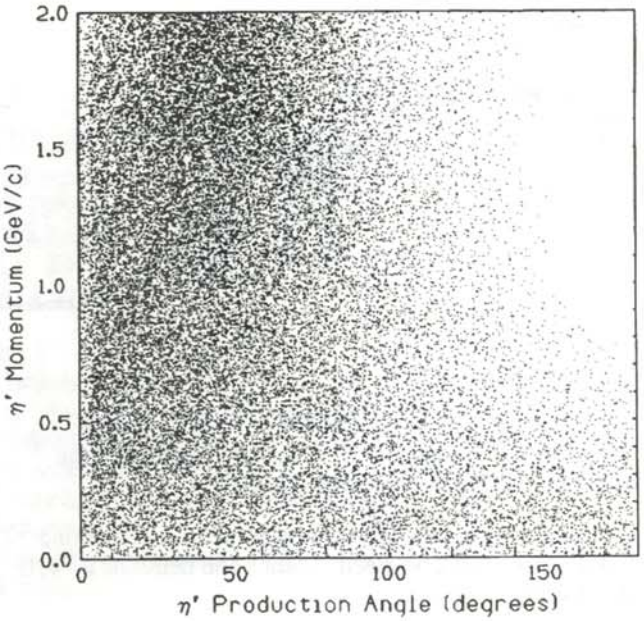

Figure 5

η' momentum versus laboratory angle for events accepted by CLAS from a uniform distribution

SIMULATIONS

Computer simulations were performed to determine the detection efficiency and the quality of particle identification one can expect for these events with the CLAS. The simulations were performed using the Monte Carlo kinematics code Charm. [5] This software simulates interactions which conserve energy and momentum, while producing events with a random distribution in the ϕ and θ angles in the center-of-mass frame of reference.

Figure 5 shows one of the results of the simulations. This plot shows the expected ability of the CLAS to detect η' mesons with various momenta and trajectories. The CLAS seems to have greatest sensitivity to those η' particles with high momentum and small angles. As shown in Figure 6, we also found that the mass spectrum recon-

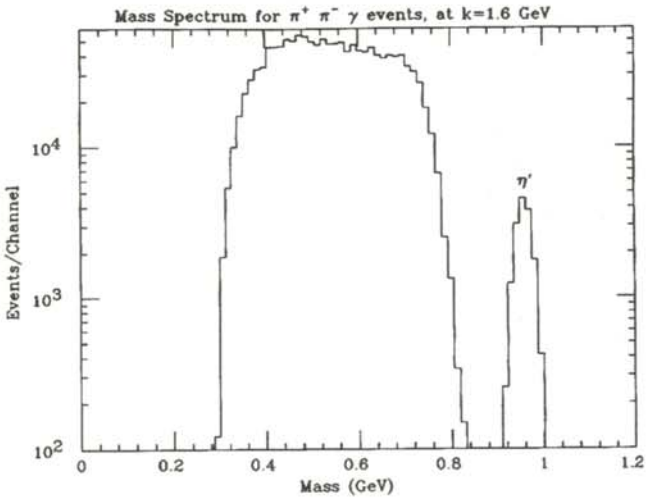

Figure 6

Reconstructed mass spectrum for an incident photon energy of 1.6 GeV, using two pions and a photon. Note that the scale of the y-axis is logarithmic.

structed from the detected $\pi^+\pi^-\gamma$ particles has a clear peak at the η' mass. The reason that there is so little background interference is that for most of the incident photon energy range, the η' is the heaviest meson that can be both photoproduced and has a high branching ration into the decay modes whose final state particles includes a π^+, a π^- and a γ. In addition, the mesons that can decay in the $\pi^+\pi^-\gamma$ mode almost always produce more than just those three particles in the final state. Since the mass reconstruction uses only these three particles, the mesons that produce more than three show up below their actual mass on the mass spectrum, which puts them far enough removed from the η' as not to interfere too much. This mass spectrum does not contain interference from accidental coincidences, but this contribution is expected to be small, as a result of the high duty factor of the accelerator. The simulations also indicate that the detection rate is greater than 12% for all incident photon energies within our range of interest.

COUNT RATES

The probability of an incident photon photoproducing an η' which then will be detected, is jointly proportion to the number of "scattering centers" (in this case, the number of nucleons) per unit volume, the η' photoproduction cross section (σ), the $\eta' \rightarrow \pi^o + \gamma$ branching ratio (BR) and the detection efficiency (ε). The expected count rate, as a function of incident photon energy, is:

$$R(k) = N_\gamma(k) \cdot \frac{N_A}{A} \cdot \rho\tau \cdot \sigma \cdot BR \cdot \varepsilon \qquad (3)$$

where $N_\gamma(k)$ is the number of photons incident on the target material at energy k, N_A is Avogadro's number, A is the atomic weight of the target whose thickness is τ and density is ρ. The bremsstrahlung photon tagger will produce a total flux of 10^7 photons/second, with an energy distribution that falls as $1/k$. We assume that $\rho\tau$, the areal target density, is 1 gm/cm^2. This is the target mass behind each square centimeter that is presented to the beam. Since there are not a lot of data on the η' photoproduction cross section, we had to estimate based on known values [6] of the η and η' cross sections at various energies. The cross section we arrived at is a constant 1mb (1×10^{-30} cm^2) over the entire range of 1.5 to 2.2 GeV. In addition, the cross section is also a function of A, the number of nucleons in the nucleus. For purposes of these calculations, we used information about the η meson, and have guessed that the cross-section should be proportional approximately to $A^{0.8}$. The branching ratio for the reaction $\eta' \rightarrow \pi^o + \gamma$ is $.300 \pm .015$. [4] For the detection efficiency, we used a conservative 12%, which is slightly lower than what our simulations yielded.

Table 1 shows our count rate estimates for various targets for two incident photon energy bins of 100 MeV. The first two columns are the predicted counts for the lowest and highest energy bins. The third is the predicted total for all the bins. Each column has units of events/sec. On a target of deuterium (A=2), our calculations estimate that we can expect .188 detected events/second, which would mean 1.02×10^5 detected η' decays over 150 hours of beam time.

SUMMARY

With a reasonably high detection rate and an excellent signal-to-noise ratio, this experiment appears to be quite feasible. Because the particle identification is good, and the count rate high, we can expect that this experiment would provide a large amount of η' photoproduction data in a reasonable period of time. When these data are compared with η' photoproduction measurement on hydrogen, information will be extracted about the nature of the η'-nucleon interaction, and thus about the structure of the η' meson.

ACKNOWLEDGMENTS

The author would like to thank Dr. Vineyard for his support, encouragement and guidance in this project and in others. This work was supported by the US Department of

Target	Rate for 1.5 - 1.6 GeV bin	Rate for 2.1 - 2.2 GeV bin	Total Detection
^{2}H	.0312	.0232	.1880
^{3}He	.0296	.0216	.1736
^{4}He`	.0280	.0192	.1640
^{12}C	.0224	.0160	.1320
^{58}Ni	.0160	.0112	.1304

Table 1

η' photoproduction count rate estimates on various nuclear targets. The second column is the lowest incident photon energy bin, the thaird column the highest. The last column is the total of all the different energy bins. The units for all entries are events/second.

Energy under contract number DE_FG05-88ER40459.

REFERENCES

1. F. Lenz, Nuc. Phys., B279 (1987), p. 119.
2. B.G.Ritchie, CEBAF proposal PB-91-008, submitted 30 Sept. 1991.
3. R.M. Baltrusaitis, et.al., Phys. Rev. D, (1 December 1985), p. 2883.
4. Particle Properties Data Booklet, June 1992, p. 21.
5. B.A.Mecking, private communication.
6. See compilation by G. Genzel, P. Joos, and W. Ffeil, Photoproduction of Elementary Particles, Landolt-Borstein, New Series I/8, (Springer, New York, 1973), p. 278;compilation by R. Baldini, et. al., Total Cross Sections for Reactions of High Energy Particles, New Series I/12b (Springer, New York, 1988), p. 361.

FACULTY SPONSOR

Dr. Michael F. Vineyard
Department of Physics
University of Richmond
Richmond, VA 23173

ANALYSIS OF WATER SAMPLES USING PARTICLE-INDUCED X-RAY EMISSION

Manakan B. Srichai*
Department of Physics and Astronomy
Arizona State University
Tempe, AZ 85287-15404

received Dec 2, 1993

ABSTRACT

Particle-induced X-ray emission analysis using 2 MeV protons was performed on a variety of filtered and evaporated water samples from the Phoeniz, Arizona area to measure the concentration of impurities present. Elemental identification was made by measuring the characteristic X-ray energies emitted by the irradiated samples. Standards were used for calibration of our measurements allowing quantitative measurements of elemental concentration.

INTRODUCTION

The major focus of the work was to determine the feasibility of utilizing particle-induced X-ray emission (PIXE) as a method for accurate, efficient water analysis. Samples were analyzed to determine the content of potentially harmful contaminants. Tap water was analyzed mainly to determine the lead content, while waters from nearby canals were analyzed for trace concentrations of other contaminants, such as arsenic and cadmium which may have been introduced through the sewage system from industrial discharge.

In PIXE, developed in the 1970's, a beam of MeV energy protons is directed onto a sample, exciting the atoms by knocking out inner-shell electron. As the atoms de-excite and the vacancies are filled by outer-shell electrons, characteristic X-rays are emitted whose energies identify the particular excited atom. [1] K_α and K_β X-rays are produced when a K-shell vacancy is filled with an electron from the L- or M- shells respectively. These photons produce the K lines in the spectrum. When the X-ray photon comes from a vacancy in the L shell, it produces the L lines in the spectrum. However, an ionized atom with a vacancy can loose also its excess energy by emitting an electron by the Auger effect [2] or similar, but more complex effects. This contributes to the complexity of PIXE analysis.

Manakan is a 1994 graduate of the Massachusetts Institute of Technology, where she received her S.B. in chemical engineering. Currently, she is attending West Virginia University School of Medicine. Manakan did this work during the summer after her junior year where she was involved in a Physics Research Experience for Undergraduates program at ASU. Her interest in this work stemmed mainly from RBS research performed previously.

The characteristic X-ray peaks present in a PIXE spectrum are superimposed on a continuous proton and secondary electron bremsstrahlung spectrum of X-rays caused by the deceleration of the projectile proton and the deceleration within the target of the electrons ejected from the atoms. An advantage of PIXE over electron beam techniques is that it uses a proton beam, which has a larger projectile mass,, and consequently small acceleration of the proton, produces a smaller bremsstrahlung background. This allows for better detection of elemental peaks within a typical spectrum.

Other advantages of PIXE analysis are that it is usually nondestructive to specimens, has excellent elemental sensitivity (sometimes on the order of parts per million) and offers greater separation and identification of high Z elements than techniques such as Rutherford backscattering spectrometry.[1]

EXPERIMENTAL PROCEDURE

Apparatus

A 2 MeV proton beam with a current between .5 and 3 nA was produced in a tandem accelerator and impinged onto the samples. The entire beam line and sample chamber were under a vacuum, typically 10^{-4} Pa.

The X-ray detector used was a lithium-drifted silicon detector Si(Li) placed at an angle of 45° to the incident beam direction. When placed under a voltage bias, the detector produces an electrical pulse with magnitude proportional to the X-ray energy. [3] A thin beryllium window was placed in front of the detector to absorb the

lower X-ray energies produced by atoms with Z < 12 and to reduce the intensity of the lower energy electron bremsstrahlung, which can account for a large fraction of the overall counting rate of the detector. The Si(Li) detector allows a high data accumulation rate and the simultaneous analysis of many elements. It has good energy resolution, typically 160 eV for a 5.9 keV peak, and high efficiencies in the 2 - 20 keV X-ray energy region. [1] The efficiency, however, falls off rapidly at energies above 30 keV, the X-ray energy for some of the higher elements.

Sample Preparation

Because the entire sample chamber was under vacuum, it was necessary for the samples to be dry. The water was removed from the samples by two methods: filtering and evaporation. Water samples were filtered though polycarbonate filters with an average pore diameter of 4 μm, thus allowing the collection of particulates contained in the water. Polycarbonate was used because its elemental composition is hydrogen, carbon and oxygen, all with Z < 8, whose characteristic X-rays are shielded by the beryllium shield . Therefore, no additional X-ray peaks were introduced due to the presence of the filter.

Because the polycarbonate filters were very thin and porous, the incident proton beam could penetrate onto the underlying metal sample holder, resulting in the presence of undesired X-ray peaks in the spectrum. To alleviate the problem, the filters were placed on Si wafers through which the proton beam could not penetrate. A 69 μm mylar film was then placed in front of the X-ray detector to reduce the transmission of X-ray energies below 2 keV. The mylar allowed better detection of elemental X-ray peaks by reducing the intensity of Si pileup peaks in the spectrum in the region between 2 keV and 5.1 keV.[1]

Since filtering was inadequate for collecting free ions, such as lead, an alternative sample preparation was used. In this technique, water samples of approximately 30 ml were collected in small plastic vials, placed open in a clean laminar flow hood, and allowed to evaporate for several days, collecting ions and particulates on the bottom of the vial. The plastic consisted of low Z elements, so it added no extra peaks to the water spectrum.

RESULTS

Method of Analysis

A typical PIXE spectrum contained overlaps of the various K lines of the lower Z elements and the L lines of the higher Z elements, thus adding to the complexity of each PIXE spectrum. To separate the peaks required sophisticated spectrum fitting techniques to extract the intensities of the principal lines for each of the elements in the sample. The PIXE spectra generated were quantitatively analyzed with a commercial software package called GUPIX. [4] The fitting procedure used a standard Marquardt nonlinear least-squares fit. [6] The experimental data are digitally filtered to subtract the bremsstrahlung and compared to a filtered model spectrum. The least squares procedure is a comparison of spectrum curvature. The fit is tested by a reduced chi-squared value.

Calibration

PIXE spectra were generated using metal standards (aluminum and steel alloys) and analyzed.[7] Comparison of the results of the elemental concentrations to published concentrations are listed in Tables 1 and 2. A typical spectrum is shown in Figure 1. The fitted data include only the elemental peaks with the continuous bremsstrahlung filtered out. The uncertainty given in Tables 1 and 2 represents the range of concentrations in parts per million (ppm) calculated for the element. The relative concentration values were converted to absolute values by assuming the relative Cr concentration in the 4340 steel standard to be accurate and normalizing the values with it. Some of the element concentrations found by the GUPIX program corresponded well to the standard values, while others resulted in large discrepancies. The normalization value was kept constant throughout the analysis. Therefore, the relative elemental concentrations found in the remaining analyses are probably more accurate than the absolute values.

To determine the accuracy of the PIXE analysis, we performed both PIXE and RBS on the two different standards. RBS analysis has been shown to be fairly accurate in quantifying the concentrations of known standards. We made two standards : 1) a 900 Å layer of Al deposited onto a 250 Å layer of Pd; 2) a 2020 Å layer of Al deposited onto a 840 Å layer of Fe. Both were sputtered onto a SiO_2 on Si substrate. Figure 2 the results for

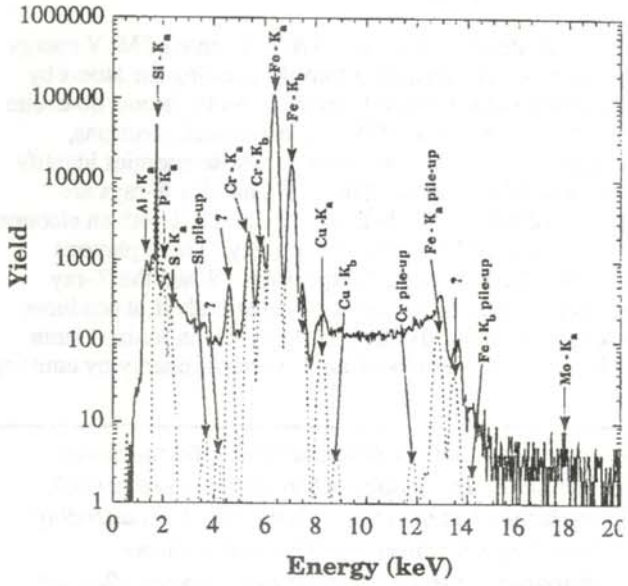

Figure 2

Digitally filtered data model spectrum (dotted line) and raw data obtained with the 4340 steel standard without mylar X-ray filter.

the Al/Fe standard. We had some problems of blocking due to the X-rays from Si. The Pd lines were in the region where the Si(Li) detector was less sensitive. These peaks were relatively weak and analysis did not detect them.

RBS analysis showed an additional heavy element peak corresponding to neither Al or Fe in the Al/Fe standard. A scanning electron microscope analysis showed contamination on the ideally smooth surface of the standard. A qualitative analysis of the PIXE spectrum shown in Figure 3 revealed the unknown contaminant to be Au. However, the quantitative analysis did not detect the L line of Au and the software program presently does not analyze the M line peaks. Table 3 shows the comparison of the analysis of the RBS and PIXE spectra of the Al/Pd and the Al/Fe standards.

The Experiment

Tap water from a Tempe Arizona household faucet was analyzed. Atomic absorption spectroscopy showed it to have approximately 3.6 parts per billion (ppb) lead and 12 ppb of copper. [8] This was probably due to leaching from the lead alloy solder and copper pipes. The faucet was left closed overnight to allow the tap water to sit in the pipes for approximately 8 hours. The first sample (Sample 1) represents the first 30 ml of water emerging from the faucet. Sample 2 was drawn from water emerging from the faucet a few seconds after opening, perhaps a more representative sample of the water sitting in the pipes. Sample 3 was collected after the faucet ran for several minutes, when the household plumbing system was flushed. All samples were evaporated onto the bottom of a plastic vial, collecting all particulates and ions which had not vaporized into the air such as chlorine.

Figure 3 shows the PIXE spectrum generated on the three

	Concentrations found from analysis			
	No mylar	69μm mylar		Ratio[b]
	$\chi^2 - 172$	$\chi^2 = 6.43$	Metals Handbook	Experiment
Element and Line	Concentration	Concentration	Concentration	Predicted
Si-K	11000 ± 4000	310000 ± 10000	4000-8000	≈ 5
Cu-K	0 ± 0	11200 ± 400	1500-4000	≈ 4
Mg-K	0 ± 0	[a]	8000-12000	-
Cr-K	3700 ± 200	7100 ± 200	400-3500	≈ 1
Fe-K	0 ± 0	15200 ± 400	7000 maximum	0
Mn-K	0 ± 0	1200 ± 200	1500 maximum	≈ 1
Zn-K	0 ± 0	900 ± 200	2500 maximum	≈ 1/3
Ti-K	0 ± 0	1800 ± 100	1500 maximum	≈ 1
Co-K	1800 ± 200	0	0	-

[a]Concentration found > 1000000

[b]Experimental concentrations from the filtered spectra were used in calculating ratios

Table 1

Results of elemental concentrations found from analysis of Al alloy 6061 standard. Concentration values are given in parts per million.

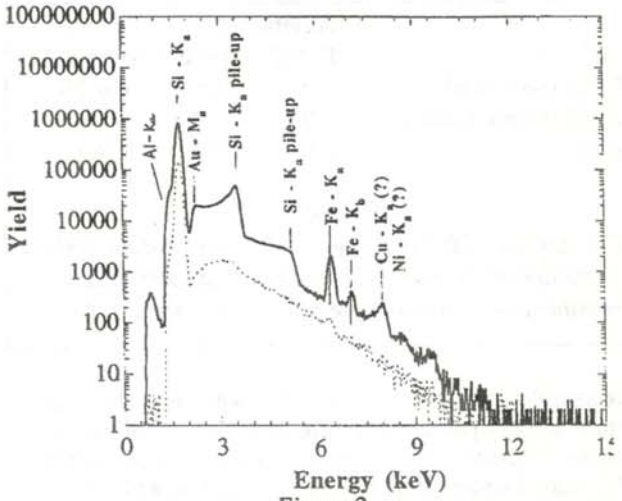

Figure 2

Raw PIXE spectrum from Al/Fe film deposited on SiO2 standard. The dotted lines are with the mylar filter and the solid line is without the filter.

water samples. They all have similar shapes. Table 4 shows the quantitative results. There is a trend for the concentration of impurities to increase from sample 1 to sample 2, but to decrease more significantly from sample 2 to sample 3. Sample 2 had the highest concentration of impurities as we expected since it was more representative of the water that had been sitting in the pipes overnight. Neither the spectra or the results of analyses on them show the presence of lead or copper impurities. These small peaks were hidden in the background noise, well below the detection limit of the Si(Li) detector for these particular elements.

Table 5 shows the PIXE results on water from two different Phoeniz, Arizona area canals. The concentrations are in parts per billion. The filtered canal water was forced

	Concentrations found from analysis		
	No mylar		
	$\chi^2 = 178.83$	Metals Handbook	Ratio
Element and Line	Concentration	Concentration	Calculated/Handbook
C[a]	-	3800-4300	-
Mn-K	7430 ± 10	6000-8000	≈ 1
Si-K	76900 ± 500	1500-3000	≈ 20
Cr-K	8200 ± 100	7000-9000	≈ 1
Ni-K	13600 ± 600	16500-20000	≈ 1
Mo-K	0	2000-3000	≈ 0
P-K	4000 ± 100	350	≈ 10
S-K	900 ± 70	400	≈ 2

[a]C peaks not present in PIXE spectra due to absorption by Be window ($Z = 6$)

Table 2

Results of elemental concentrations found from analysis of 4340 steel standard. Concentrations are given in parts per million.

	Atomic Ratio		Possible
	Pd/Al	Al/Fe	Contaminants
PIXE (no mylar)	0	0.5	Cu, Ni
PIXE (69mm mylar)	0	≈ 0	-
RBS	0.31	0.59	Pt, Au, W

Table 3

Comparison of PIXE analysis, RBS and SEM analysis on Al/Pd and Al/Fe sputtered onto SiO2 samples. The possible contaminants were on the Al/Fe standard.

For sample 1, the water was filtered onto polycarbonate filters, so only particulates were collected. Analysis was performed using a Si backing and mylar detector shield. The second water sample was evaporated in a plastic container. Since the plastic sample substrate was made of an insulating material, a slight electrical charging of the sample was observed during analysis. The subsequent electrical breakdown of built up charge on the sample added significantly to the background noise, thus decreasing the intensity of the elemental peaks in the range 4 keV and higher. Figure 4 shows the PIXE spectra of the two water samples.

DISCUSSION

One of the difficulties encountered with the water analysis was obtaining a representative sample of the water. Since some of the samples represented only a small volume of water (≈30 ml), probably only a very small amount of material deposited onto a relatively large surface was sampled. Because of the inhomogeneity of the sample, the small area analyzed by the proton beam may not have been representative of the overall composition of the samples.

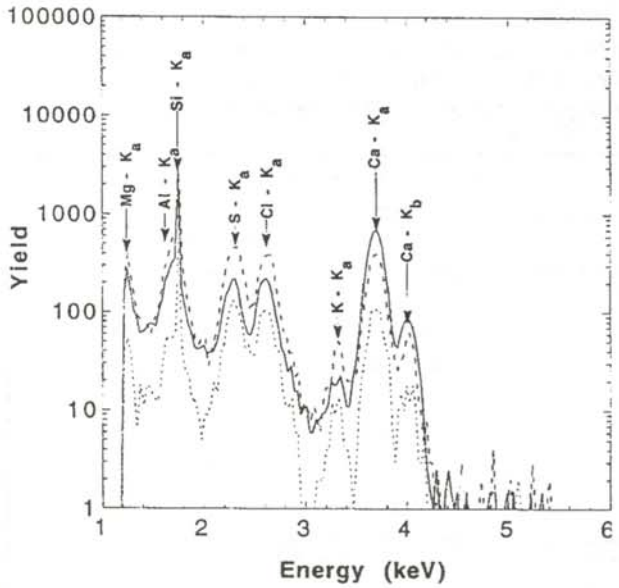

Figure 3

Raw PIXE spectra from the three tap water samples. Samples 1, 2 and 3 are represented by the solid, dashed and dotted lines, respectively.

	Concentration in ppb		
	Sample 1 $\chi^2 = 9$	Sample 2 $\chi^2 = 2.5$	Sample 3 $\chi^2 = 0.8$
Mg	4.5±0.8	33±1	5.0±0.6
Al	11.3±0.6	13.2±1.3	2.5±0.6
Si	98±2	105±3	17.6±1.2
P	6.9±0.6	0	0
S	18.2±0.6	76±2	18.2±0.6
Cl	37.1±1.3	76±2	19±1
K	1.3±0.6	12.6±1.3	3.8±0.6
Ca	230±3	147±3	39±2
Fe	0	0	0
Cu	0	0	0
Pb	0	0	0

Table 4

Concentrations in parts per billion determined by PIXE of Tempe Arizona drinking water. All data use the K line except for the Pb data.

Elemental concentration analyses on the calibration standards showed significant deviation from the concentrations given in the metals handbook. The standards used were relatively thick, and the poor correlations obtained ($\chi^2 > 1$) were due to the great complexities in analysis of PIXE spectra obtained from thick films. The problems encountered with the Al/Pd and Al/Fe standards probably resulted mostly from the need for better standards. Preparation of the standards was a problem as seen from the contamination of the Al/Fe standard. Another difficulty with the standards was that the 1.74 keV Al and 21.2 keV Pd K_α peaks lie outside the energy range where the Si(Li) detector is most efficient. Because these were thin films, sputtered onto a thick SiO_2 substrate, the amounts of Al, Pd, and Fe sampled relative to Si were quite low, resulting in less intense energy peaks. Further, the Si peak interfered with the Al peak, complicating the spectrum analysis even more. A better standard for future work would be to use elements in the region of Z between 33 and 44, deposited on a low Z substrate such as silicon. This would produce a spectrum containing the more intense K-lines in the most efficient detection range of the Si(Li) detector.

While lead is known to be present in the tap water sampled, the absence of lead in the analysis probably resulted from the poor sensitivity of the Si(Li) detector to the M-line energy peaks of Pb. The M-line peak was used (≈2.6 keV) since the K- and L- line peaks energy are too high to be detected. In addition, the small volume of water sampled probably contained only trace amounts of lead, below the detection limit of the Si(Li) detector.

The correlation between the fit and the data were better for

	Concentration in parts per billion	
	Filtered Canal Water 69 μm mylar $\chi^2 = 0.8$	Evaporated Aquaduct Water No mylar $\chi^2 = 67$
Na	0	1.4±0.2
Mg	0	0
Al	(22.0±0.6)x10⁴	145.6±2.5
Si	(42.6±0.2)x103	630±6
P	21±16	27.8±2.5
S	15±2	92±9
Cl	8±1	1449±6
K	159±2	25±4
Ca	300±3	1526±6
Cr	2.0±0.5	0
Mn	6.8±0.5	2.9±5.7
Fe	233±2	8.8±6.3
Co	2.5±1.3	0
Ni	0.8±0.4	0
As	0	0
As (L - line)	a	145±1
Rb	0	0
Rb (L - line)	0	137±7
Sr (L - line)	(3.6±1.8)x 102	0
Mo	0	0
Mo (L - line)	0	396±3
Cd	0	0
Cd (L - line)	0	5.0±3.8

Table 5

Concentrations in parts per billion of impurities found in canal waters as determined from PIXE analysis. The analysis used the K - line unless otherwise indicated.

the water samples than the standards. Some of the concentrations were higher than one part per thousand. This is because the normalization value used was found by assuming the relative Cr concentration found experimentally in the 4340 steel standard to be accurate. A more accurate value for the normalization could have been found by measuring the solid angle from the sample to the detector [5], but this measurement was not made for this work.

ACKNOWLEDGMENTS

The author thanks Robert J. Culbertson, Barry J. Wilkens and James W. Mayer for their guidance and support. She also acknowledges Lawrence C. McEntyre and Donald Ashbough at the University of Arizona and Randal Appleton at Arizona State University for technical support with the GUPIX software. This work was performed under the auspices of the Arizona State University Physics Research Experience for Undergraduates Program, supported by the National Science Foundation and Arizona State University.

REFERENCES

* Present address of author: 3557 Collins Ferry Rd., Apt D14, Morgantown, WV 26505.

1. S.A.E. Johansson and J. Campbell, P.I.X.E. A Novel Technique for Elemental Analysis, John Wiley and Sons, 1988.
2. B.D. Cullity, Elements of X-Ray Diffraction, Addison-Wesley Publishing Company, Inc., 1978.
3. L.C. Feldman, J.W. Mayer, Fundamentals of Surface and Thin Film Analysis, Elsevier Science Publishing Co., Inc., 1986.
4. J.W. Mayer, E. Rimini, Ion Beam Handbook for Material Analysis, Academic Press, New York, 1977.
5. J.A. Maxwell, J.L. Campbell and W.J. Teesdale, Nucl. Instrum. Methods, B43, 1989, p. 218.
6. P.R. Bevington, Data Reduction and Error Analysis for the Physical Sciences, McGraw-Hill, New York, 1960.
7. Metals Handbook, Ninth Edition, American Society for Metals, 1978.
8. B. Olivieri, City of Tempe, January, 1993 (unpublished).

FACULTY SPONSOR

Dr. Robert J. Culbertson
Department of Physics and Astronomy
Arizona State University
Tempe, AZ 85287-1504
Culbertson@phyast.la.asu.edu

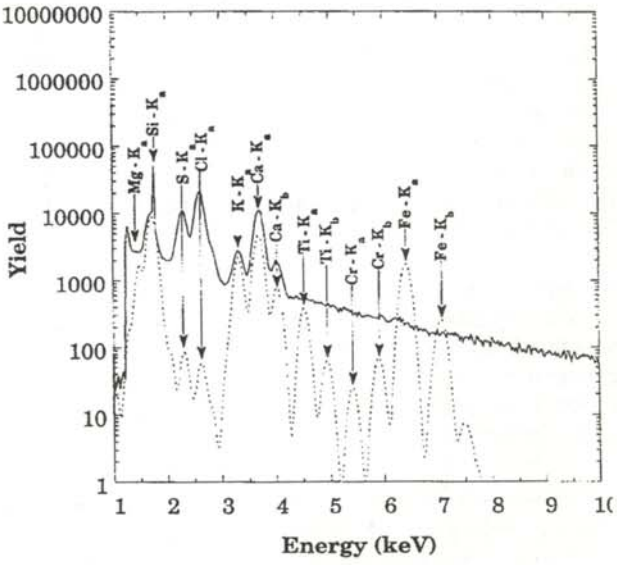

Figure 4

Raw PIXE spectra from both the filtered (dotted line) and evaporated (solid line) canal water. The large background in the latter spectrum resulted from the electrical breakdown of built up charge on the sample during data acquisition

THE MODELING OF PHOSPHORUS DYNAMICS IN A LAKE SYSTEM

Todd N. Swift *
Physics Department
University of Northern Iowa
Cedar Falls, IA 50614
received January 5, 1994

ABSTRACT

We constructed a basic closed stock and flow model of lake phosphorus cycling that includes three stock concentrations: inorganic phosphorus, phosphorus in living organic material and phosphorus in dead organic material. The stocks are connected by flows that are made stock dependent in a plausible manner. The model exhibits two equilibrium points, one stable and the other unstable, with an interesting crossover between them. Below a certain total phosphorous threshold, stable equilibrium is characterized by all of the phosphorus stock residing in the inorganic form, suggesting the collapse of the biological system. Above the threshold, this is not true. We then used STELLA®II, a computer program for dynamic modeling, to study the dynamics of the basic model as well as some extensions and modifications such as the addition of another stock and external loading of the system. When the system was perturbed from equilibrium, the model showed eutrophication blooms and other interesting behavior.

INTRODUCTION

The element phosphorus is essential to the growth of all plants, including algae. Phosphorus is often not freely available in natural waters. It is one of the elements whose availability is a major constraint on the production of large crops of plankton algae. [1] When large amounts of phosphorus are added to a lake, algae grow rapidly in a process called eutrophication. When these algae exceed the carrying capacity of the lake and die out, the bacterial that thrive on their decay consume large amounts of oxygen. This can kill fish in the lake.

The implications of human disruption of the phosphorous cycles in populated lake areas are not always clear. Small amounts of additional phosphorus may be beneficial, but large amounts may be disastrous. The biological cycling of phosphorus and the attendant disruptions can be extremely rapid. [1]

Todd, currently a graduate student in mechanical engineering, works at the Solar Energy Applications Laboratory at Colorado State University in Ft. Collins. The research in this paper was completed for his senior project leading to a B.S. in Applied Physics at the University of Northern Iowa in Cedar Falls. In his spare time, Todd enjoys mountain activities in the Colorado Rockies

We developed a basic model for the phosphorus cycle in a lake and studied its behavior under various conditions. Dynamic modeling of biological systems is an important activity in many areas, ranging from terrestrial environmental science to closed life-support systems in space vehicles. The mathematical modeling of space biological systems may become more important as the length of time that astronauts spend in space continually increases, while the weight of the resources that may be used for life support remains constrained.

THE BASIC MODEL

The basic model [2] is a very simple closed box model of the interrelationships of phosphorus concentrations in living organic matter (L), inorganic matter (P) and dead organic matter (D) in a lake. The dimensional equations for the basic model are: [2]

$$\frac{dL}{dt} = \beta P L - \gamma L \qquad (1)$$

$$\frac{dP}{dt} = \alpha D - \beta P L \qquad (2)$$

$$\frac{dD}{dt} = \gamma L - \alpha D, \qquad (3)$$

where t is the time and representative values of the rate constants α, β and γ are 0.05/day, 2.5/(day μM) and 0.25/day respectively. To reduce the number of rate constants and thereby reduce the complexity of Equations 1-3, we

introduce dimensionless variables by setting:

$$L=\frac{\gamma}{\beta}L',\ P=\frac{\gamma}{\beta}P',\ D=\frac{\gamma^2}{\alpha\beta}D',\ t=\frac{1}{\gamma}t'. \qquad (4)$$

Substitution of the expressions of Equation 4 into Equations 1 - 3, simplifying and dropping the prime notation yields:

$$\frac{dL}{dt}=PL-L \qquad (5)$$

$$\frac{dP}{dt}=D-PL \qquad (6)$$

$$\frac{dD}{dt}=cL-cD, \qquad (7)$$

where c is a dimensionless rate constant equal to α/γ. Since c does not depend on β, β enters into the dynamics of the system only through its effect on the initial values of the dimensionless variables. Figure 1 shows the model in its dimensionless form. The conversion to a dimensionless form requires that the flows into and out of the D box be unit converted.

In a closed lake system, the amount of phosphorus must be conserved. This is seen in the dimensional equations (Equations 1-3) by summing the right-hand sides of all three equations and noting that the result is zero. In the dimensionless variables adopted here, conservation of the amount of phosphorus implies that:

$$L+P+\frac{D}{c}=K, \qquad (8)$$

where K is the dimensionless total phosphorus concentration in all forms.

ANALYTIC STUDY OF THE BASIC MODEL

The three governing equations (Equations 5 - 7) can be reduced to two to facilitate analysis. By using Equation 8 to eliminate D in Equation 6, we arrive at the two governing nonlinear equations for L and P:

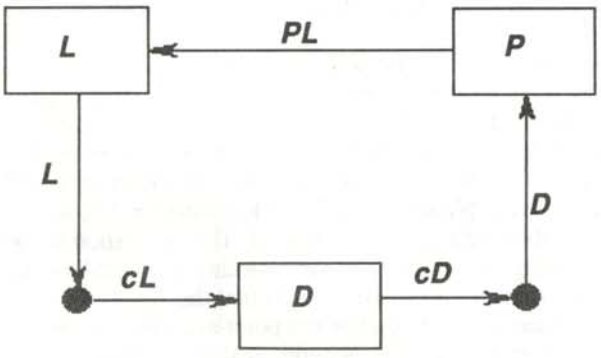

Figure 1

Diagram of the basic model, where the boxes labeled L, P, and D represent dimensionless concentrations of phosphorus in living organic material, inorganic material, and dead organic material, respectively, and c *is a dimensionless rate constant. The dark circular areas represent single unit converters.*

$$\frac{dL}{dt}=PL-L \qquad (5)$$

$$\frac{dP}{dt}=c(K-P-L)-PL. \qquad (9)$$

Values of D can then be obtained from Equation 8.

At equilibrium, L and P will be constant, so setting the right-hand sides of Equation 5 and Equation 9 to zero, the equilibrium conditions may be obtained. Two equilibrium points are found: L=0, P=K and L=$c(K-1)/(c+1)$, P=1. A linear stability analysis of each of these equilibrium points can be performed by examining the exponential time dependence of small perturbations from equilibrium. The exponents are calculated as eigenvalues, and the signs of the real parts of these determine stability. A negative sign indicates decay to the equilibrium point for long times and hence stability, while a positive sign indicates instability.

For the first equilibrium point, L=0, P=K, we find that the eigenvalues are $-c$ and $K-1$. Perturbations L^* and P^* in the neighborhood of the point are then given by:

$$\begin{bmatrix}L^*\\P^*\end{bmatrix}=W_1\begin{bmatrix}0\\1\end{bmatrix}e^{-ct}+W_2\begin{bmatrix}1\\\frac{c+K}{1-c-K}\end{bmatrix}e^{(K-1)t}, \qquad (10)$$

where W_1 and W_2 are constants determined by the initial conditions. Thus, if K<1, this equilibrium point is stable; if K>1, it is unstable. Linear stability analysis fails in the case K=1 because the two equilibrium points coalesce. We then find, by graphical means, that this single equilibrium point has both stable and unstable attributes but is stable in the domain of interest.

For the second equilibrium point, L=$c(K-1)/(c+1)$, P=1, the eigenvalues are not so easily calculated. We can show that if K<1, the equilibrium point is unstable, and if K>1, it is stable. In the latter case, solutions approach equilibrium in an oscillatory or monotonic manner depending on the value of K. Larger K values produce eigenvalues that are real and negative, resulting in a monotonic approach to equilibrium. Smaller K values result in eigenvalues that are complex conjugates of each other, resulting in an oscillatory approach to equilibrium. The condition for stability of the second equilibrium point is opposite to that for the first point.

The long-term behavior of the system depends on the single constant K, which measures the total concentration of phosphorus in the system. If it is too low, K<1, the system will eventually settle down to equilibrium at L=0, P=K. The condition L=0 means that there is no phosphorus in living organic material and suggests that the biological system has collapsed due to insufficient phosphorus. This may also mean that if we perturb a dead system (L=0) by adding sufficient phosphorus to make K>1, we can bring the system back to life (provided there is a "seed" of algae or living material to begin the growth).

Figure 2 shows the stable equilibrium point and physically admissible regions (L, P, D ≥ 0) of the LP-plane for $K<1$, $K=1$, and $K>1$. As K increases, the sloping boundary of the region moves outward from the origin while maintaining a slope of magnitude unity. When $K \leq 1$, the system will settle down to $L=0$.

STELLA II AND THE DYNAMICS OF THE BASIC MODEL

The long-term behavior of the basic model is completely determined by the analysis discussed in the previous section, but this analysis tells us very little about what the system does on its way to final equilibrium. Also, when the model is extended to improve its realism, analytic analysis becomes very difficult to perform, and we must turn increasingly to computational numeric techniques. STELLA II [3] (hereafter referred to as STELLA) is a simulation program designed to model dynamic systems in a relatively simple manner. It is powerful and has the potential to significantly lessen the programming demands for any dynamical modeling project.

Figure 3 shows the basic model as constructed in STELLA and can be used to explain the workings of the program. There are four basic building blocks used to represent dynamical systems in STELLA: stocks; flows; converters; and connectors. The rectangular boxes are *stocks* and, in this case, represent the three kinds of phosphorus. Every stock accumulates one type of phosphorus. The stocks are connected by *flows* that have "spigots" on them to control the flows. The half-shaded flow circles represent flows in which unit conversions are performed. This is needed for the dimensionless model. The cloud represents an infinite stock. In this case, there is an infinite supply of phosphorus (from the lake's point of view) that could be added to the lake to perturb it. Circles that are used to modify flows and stocks are called *converters*. There are none used in the basic model, but these can be used when more complexity is required. Finally, *connectors* are used to connect parts of the model that depend on each other. These are the curved arrows seen in Figure 3. A nonlinear term appears in the basic model because the growth rate depends on both the living phosphorus concentration and the inorganic phosphorus concentration. This can be seen by the connectors coming from both of these stocks to the growth flow.

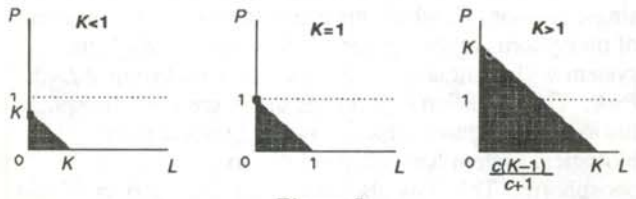

Figure 2

Stable equilibrium point, black dot, and the physically admissible region, shaded, in the L-P plane for $K<1$, $K=1$ and $K>1$.

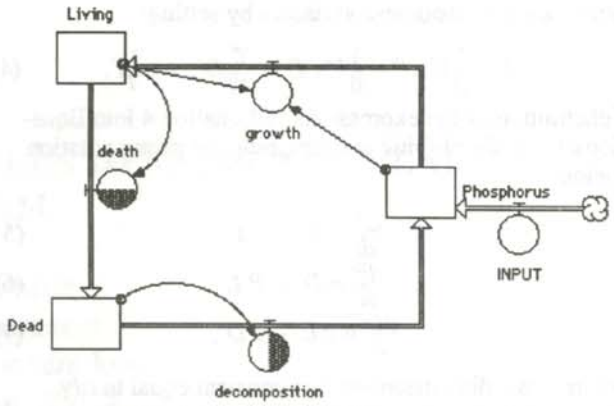

Figure 3

The basic model, as constructed in STELLA. The cloud attached to the INPUT flow represents an infinite source of inorganic phosphorus and the shaded circles represent single unit conversions.

After designing the system graphically, the user of STELLA must then define all of the quantities and relationships between the various components of the model. When this is done, the model can be run and adjusted so that it is in equilibrium. The dynamics of the model, when perturbed from equilibrium, can then be studied.

The basic model only requires initial values for L, P, and D and a value for c. The constant c acts in the unit converted flows in Figure 3 and controls the flow rate between the appropriate stocks. The value used for c was 0.2, which is realistic for a lake system. In the dimensionless model, the L, P, D point of 1,1,1 (which corresponds to $K=7$) is a stable equilibrium point. We started with all three of the stock concentrations at unity and then perturbed the system using a STELLA function called "pulse" to rapidly increase the concentration in the inorganic phosphorus stock to a new value. The added phosphorus came from the infinite cloud of phosphorus.

One way that lakes are perturbed is by the phosphorus from fertilizers and detergents that are commonly used today, so we begin by simulating a perturbation of this sort. When we perturb the system by adding a pulse of height 0.5 (a 50% increase) and width of one time step to the inorganic phosphorus (P) stock at time $t = 3.0$, we obtain the result shown in Figure 4. The simulation shows oscillating concentrations, overshooting their equilibrium values several times. This means that the eigenvalues associated with the equilibrium point are complex conjugates of each other with negative real parts. Figure 5 shows the solutions when we pick an extremely large initial perturbation that results in a K value of 50. Here we obtain solutions that monotonically approach new equilibrium values.

EXTENDING THE MODEL

Any realistic model of the phosphorus cycle in a lake must

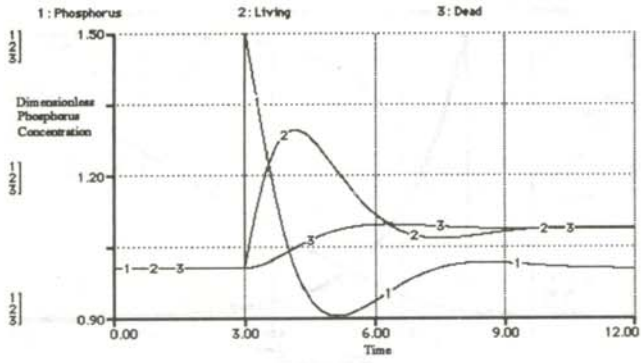

Figure 4

Results of increasing the inorganic phosphorus concentration by 0.5 units at time t=*3.0. Note the initial rapid increase in the living concentration followed by a rapid decrease to the new equilibrium values:* P=*1 and* L=D=*1.083.*

distinguish between absorption and growth. Absorption is the process by which algae rapidly absorb nutrients at a rate several times faster than they can use them to grow. The nutrients, called luxury nutrients, are "stored" until the algae can grow. To accommodate this, we modified the model to include one additional stock, called luxury phosphorus.

We first assumed that the absorption (uptake) rate, or the flow from phosphorus to luxury phosphorus was very fast. Within twenty minutes of adding H_3PO_4 to a system, more than ninety percent of the added phosphorus was incorporated into algae.[4] We chose a rate constant, ϕ, of 30/day

The second assumption was that algal growth follows the Michaelis-Menton equation.[5,6] The form of this equation is seen in the right hand sides of Equations 12 and 13. The remaining rate constants were chosen to be similar to those in the basic model. The dimensional equations are then:

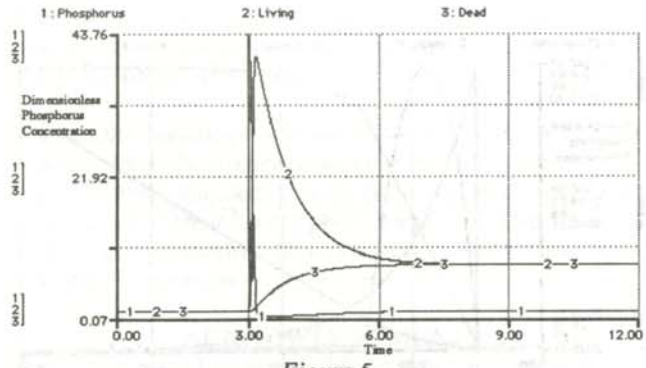

Figure 5

Results of increasing the dimensionless concentration of inorganic phosphorus by 43 units at t=3.0. Note the monotonic approach to the new equilibrium values: P=1, L=D=8.167.

$$\frac{dP}{dt} = \alpha D - \phi P \tag{11}$$

$$\frac{dLux}{dt} = \phi P - \frac{\theta\, Lux}{Z + Lux} L \tag{12}$$

$$\frac{dL}{dt} = \frac{\theta\, Lux}{Z + Lux} L - \gamma L \tag{13}$$

$$\frac{dD}{dt} = \gamma L - \alpha D\,, \tag{14}$$

where P, Lux, L, and D are the phosphorus concentrations in the respective forms, t is the time, α, γ, ϕ and θ are rate constants with representative values of 0.05/day, 0.25/day, 30/day, and 2.5/day, respectively, and Z is the luxury concentration where the growth rate is one-half its maximum value in the Michaelis-Menton relation.

Following a procedure similar to that described with the basic model, we define the following quantities to reduce the number of constant terms:

$$P = Z\,P',\ Lux = Z\,Lux',\ L = \frac{\phi^2}{\alpha\gamma} Z\,L',$$
$$D = \frac{\phi}{\alpha} Z\,D',\ t = \frac{1}{\phi} t'\,. \tag{15}$$

Substituting, simplifying, and dropping the prime notation gives us the more useful dimensionless equations:

$$\frac{dP}{dt} = D - P \tag{16}$$

$$\frac{dLux}{dt} = P - \frac{c_2\, Lux\, L}{c_1\, c_3\, (1 + Lux)} \tag{17}$$

$$\frac{dL}{dt} = c_2 \frac{Lux\, L}{(1 + Lux)} - c_3 L \tag{18}$$

$$\frac{dD}{dt} = L - c_1 D\,, \tag{19}$$

where the concentrations are now dimensionless, and c_1, c_2, and c_3 are α/ϕ, θ/ϕ, and γ/ϕ respectively.

An additional part of the new system, shown in Figure 6, is the converter LuxConstraint which constrains the concentration of phosphorus in luxury form so that it does not exceed six percent of the concentration of phosphorus in living material. In dimensionless terms, we must have:

$$Lux \le \frac{0.06}{c_1\, c_2} L\,. \tag{20}$$

The second term in the right-hand side of Equation 17 and the first term in the right-hand side of Equation 18 should be set to zero when the luxury concentration exceeds its allowable amount. This was implemented in STELLA by multiplying these terms by a function of the form:

$$\frac{1}{1 + e^{(-x/a)}}\,, \tag{21}$$

where x is the right-hand side of Equation 20 minus the left-hand side and a is a scale constant. When Lux is significantly below its maximum value in comparison to a, Equation 21 gives a value that is nearly unity. When Lux is significantly above its maximum value in comparison to a, Equation 21 is nearly zero, effectively disabling the absorption flow. Thus, a controls the range of Lux within

which the transition from full absorption to no absorption takes place.

The model was first run until an equilibrium point was established. The resulting equilibrium concentrations were then converted to their dimensional counterparts to see if the numbers were realistic. We then began perturbations of the model to see what would happen. Figure 7 shows the results of an increase of 50% (1000 units) in the concentration of inorganic phosphorus at t=1.0. The dynamics of the luxury phosphorus stock closely follow the inorganic phosphorus stock because the absorption rate constant is very large, allowing the luxury concentration to rise very rapidly. As the luxury concentration rises, the growth rate (seen as a flow in Figure 6) increases and the living concentration increases rapidly. This is followed by a decrease in the growth rate and a leveling off of the living concentration as the luxury and phosphorus concentrations are reduced close to their new equilibrium values. The living and dead concentrations are not yet in equilibrium after eight dimensionless units of time (about 6 hours of real time). The living concentration has begun to decline and the dead concentration continues to rise.

Figure 8 shows the results when the inorganic phosphorus concentration is increased by 40,000 units. There are several interesting things happening after this perturbation. The increase in luxury concentration is not as abrupt as in the previous case because there is so much more inorganic phosphorus available that, even with a very large absorption rate constant, the absorption flow takes some time to fill the luxury stock concentration to its maximum. The high rate of decrease of the luxury concentration after t=2.0 causes the concentration to become nearly zero. This may be a defect in the model. STELLA will not allow the stock to go below zero, so the luxury concentration becomes a very small number and there is a discontinuity in the growth rate. However, the growth rate is still positive showing that there is some flow into the living stock. This result seems to make sense in the real world:

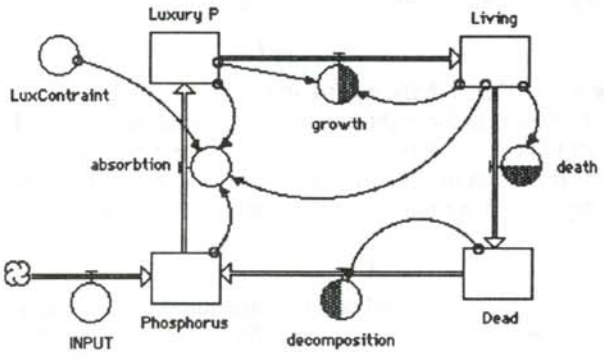

Figure 6

The model extended to include luxury phosphorus as an additional stock. The converter, LuxConstraint, is used to restrict the luxury phosphorus concentration (see text).

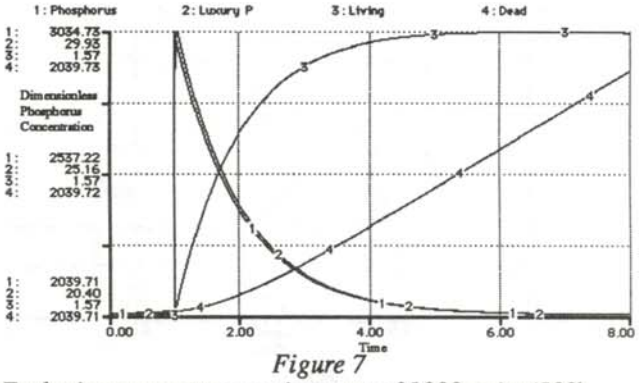

Figure 7

Early time response to an increase of 1000 units (50% increase) in the dimensionless concentration of inorganic phosphorus at t=*1.0. Note the dynamics of the luxury stock closely follow those of the inorganic stock.*

the algae deplete their luxury stock to zero and begin growing directly from the inorganic phosphorus stock. But, we are not sure how STELLA is producing this result as there is no direct connection between the inorganic and living phosphorus stocks. There are no discontinuities in the slope of the inorganic phosphorus curve, suggesting that the flow from it has not been disrupted. If the non-negativity requirement is relaxed, the curves do not have any kinks and the luxury concentration will become negative. More work needs to be done to better understand this situation.

The shape of the inorganic, living, and dead phosphorus concentration curves of Figure 8 are similar to those in Figure 7 except for the discontinuities mentioned in the previous paragraph. The living phosphorus curve does not appear to be bending over (prior to the discontinuity) as it was in Figure 7. This may be because there is more total phosphorus available, thus extending the period of rapid growth. The maximum luxury concentration constraint has not been reached in either of these situations.

Figure 9 shows the results of a perturbation that is large

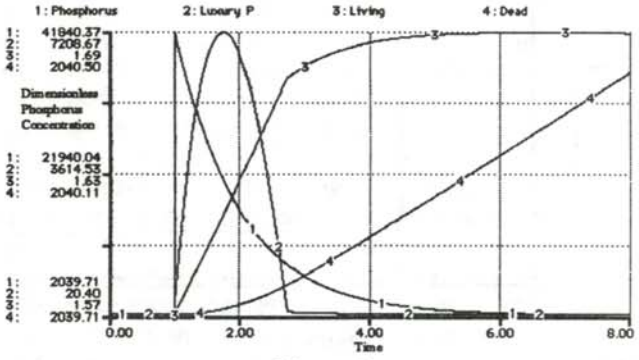

Figure 8

Early time response to an increase of 40,000 units in the dimensionless concentration of inorganic phosphorus at t=*1.0.*

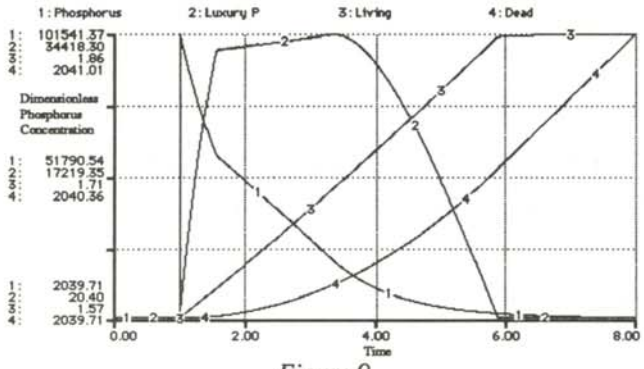

Figure 9

Early time response to an extremely large increase of 100,000 units in the dimensionless concentration of inorganic phosphorus at t=*1.0. Note the discontinuity in the luxury stock when the luxury concentration reaches its maximum at* t=*1.5.*

enough to make the luxury concentration reach its maximum allowable amount. This behavior is similar to that in Figure 8 except that at t=1.5, the luxury concentration has reached its maximum value relative to the living concentration. The constraint comes into effect as the absorption rate is rapidly decreased and the luxury concentration switches to a new path that rises as the concentration in the living stock raises the maximum allowable luxury concentration. Later, the luxury concentration nearly reaches zero, as in Figure 8, and causes a discontinuity in the growth rate.

These numerical experiments are interesting in themselves but also indicate problems that need to be solved. The model needs to be constructed in such a way that the long-term and the short-term behaviors can be observed. Unfortunately, an adaptive step size algorithm is not available in STELLA. Choosing a time step that is small enough to accurately capture the short-term dynamics currently requires too much memory to see the long-term equilibrium. One method we are attempting to use to avoid this problem is to change the time scale of the model at a point in time that we can choose. This should make it possible to include the long-term equilibrium and the early dynamics on the same graph.

Perhaps the biggest problem is discovering what STELLA is doing when the luxury concentration drops to nearly zero. We must also decide if the result we obtained, algae using up all of their luxury phosphorus, is realistic and if it is not, we must modify the model further before making any other extensions.

ACKNOWLEDGMENTS

The author would especially like to thank his research advisor, Dr. Kent Macomber, without whom this project would not have been possible. His insights and ideas kept the research going. Also, many thanks go to Dr. Ed Brown, who spent much time discussing the biological aspects of the models. Finally, the author would like to thank the Iowa Space Grant Consortium for an undergraduate research scholarship to pursue this project.

REFERENCES

* Current address of the author: 500 W. Prospect #25-B, Ft. Collins, CO 80526
TS743682@longs.lance.colostate.edu.

1. Reynolds, C. S., "Phosphorus and the Eutrophication of Lakes: A Personal View." Phosphorus in the Environment: Its Chemistry and Biochemistry, from the Ciba Foundation Symposium 57, Elsevier, New York, NY.,(1978), p. 202.
2. Harte, John, Consider a Spherical Cow: A Course in Environmental Problem Solving, University Science Books, Mill Valley, CA., (1988), pp. 45-49.
3. High Performance Systems, Inc., STELLA II software. Hanover, NH.,1992.
4. Emsley, John and Dennis Hall, The Chemistry of Phosphorus:Environmental, Organic, Inorganic, Biochemical, and Aspects, Harper and Row, New York, NY., (1976), p. 22.
5. Molot, Lewis and Edward Brown, "Method for Determining the Temporal Response of Microbial Phosphate Transport Affinity.", Applied and Environmental Microbiology, 51, (1986.) pp. 524-531.
6. Brown, Edward J., Robin F. Harris, and Joseph Koonce, "Kinetics of Phosphate Uptake by Aquatic Microorganisms: Deviations From a Simple Michaelis-Menton Equation", Limnology and Oceanography, 54, (1978), pp. 26-34.

FACULTY SPONSOR

Dr. H. K. Macomber
Department of Physics
University of Northern Iowa
Cedar Falls, IA 50614

ANALYSIS OF THE HYDROGEN-TERMINATED Si(111)-(1x1) SURFACE USING ION SCATTERING TECHNIQUES

Karl K. Vigen*
Department of Physics and Astronomy
Arizona State University
Tempe, AZ 85287-1504

received December 12, 1993

ABSTRACT

The hydrogen-terminated Si(111)-(1x1) surface was studied with both ion channeling and elastic recoil detection techniques. The Si(111)-(1x1) surface was prepared using a hydrofluoric acid/ammonium fluoride cleaning and etching process. Angular scans were performed about the [001] axis to determine if any major reconstruction normal to the surface was present. Elastic recoil detection was used to qualitatively determine hydrogen concentration at the surface. The present data suggest that very little relaxation or contraction occurs perpendicular to the surface.

INTRODUCTION

In the hydrogen-terminated Si(111)-(1x1) surface, the free bond at each silicon surface atom is terminated with hydrogen. It is a remarkable surface because it is microscopically flat over a large area, perfectly terminated with hydrogen and completely passivated. Infrared spectroscopy and scanning tunneling microscopy (STM) studies show that hydrofluoric acid and ammonium fluoride etching produces essentially flat surfaces with terraces of hundreds of nanometers across. [1] Other studies show that the hydrogen termination also leaves the surface extremely resistant to contamination.[2] However, little research has been done measuring the distances between the first several Si(111) planes of the hydrogen-terminated Si(111)-(1x1) surface. The surface is labeled (1x1) because the dimensions of the surface lattice are the same as the bulk Si lattice constant. In contrast, the surface atoms in Si(111)-(7x7) are arranged such that the dimensions are seven times the bulk Si lattice constant. Using ion-channeling techniques, one can determine whether any perpendicular relaxation or contraction occurs in the first several monolayers.

In Rutherford backscattering spectrometry (RBS), ions are accelerated and directed onto the target samples, where they interact with the target atoms. Common ion species include He++, and H+, which are usually given energies between 0.5 and 4.0 MeV. If an incident ion is less massive than the target atom, the incident particle will backscatter with an energy characteristic of the masses of the particles, the backscattering angle, and the depth at which the incident ion scatters [3]. For an amorphous material or a crystalline material which is not aligned with the incident beam, a spectrum such as the one marked 'random' in Figure 1 is obtained. The sharp right edge of the spectrum indicates the ions scattered from the surface

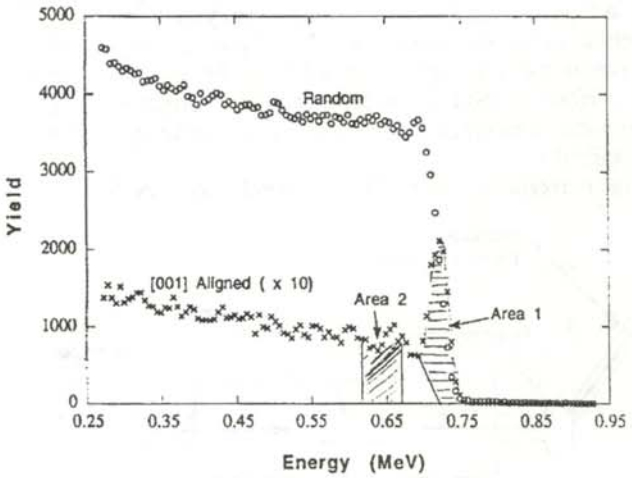

Figure 1

Representative 'random' (o) and 'aligned' (x) spectra for He+ ions incident on a Si(111) surface. The 'aligned' spectrum is taken for the [100] axial direction and is magnified 10 times. Area 1 is the surface peak (A_{SP}). Area 2 is the area of minimum yield directly behind the surface peak.

Karl K. Vigen is a senior physics major at Gustavus Adolphus College. This work was done during the summer of 1993 at Arizona State University. In his free time, Karl enjoys singing, and playing racquetball and basketball. He plans to pursue graduate studies in physics or medical physics.

of the material. As the ions penetrate the target, they lose energy (primarily through interactions with the electron clouds of the target atoms) and are scattered at lower energies.

For crystalline solids, such as silicon, the target sample can be aligned such that the incident ion beam is parallel to a crystal plane or axis in a process called ion channeling. The atoms appear ordered as rows parallel to the incident beam direction. The first atom in each row helps to shield, or shadow, deeper atoms from the incident ions. Because a small number of incident ions become misaligned, or dechanneled, once inside the target and the target atoms vibrate about their lattice sites, the underlying atoms in a particular row are not perfectly shadowed. Thus, the channeling spectrum, as shown in Figure 1, has a peak at the surface, due to scattering from the first few atoms in each row, and a reduced yield at lower energies.

The surface peak gives a measure of the areal density of the target surface layer and thus the shadowing effect that occurs. If atoms are reconstructed on the surface of the target, the surface peak for different axial orientations of the crystal can be used to measure the extent of this reconstruction.[3,4] The size of the surface peak is calculated by summing the total counts under the peak and subtracting a background number of counts to obtain Area 1 in Figure 1. The surface peak is generally given in units of atoms/cm^2 or atoms/row for a given crystal structure and orientation. For example, silicon has a lattice constant of 0.543 nm and crystallizes in the diamond structure, so there are 2.71×10^{15} [001] rows/cm^2.

The incident beam angle, θ_o, can be rotated about the channel axis in small increments. The surface peak (Area 1 in Figure 1) and the area of minimum yield directly behind the surface peak (Area 2 in Figure 1) are plotted as a function of angular divergence from the axis. If the scan is performed about a non-normal axis, information about atomic displacements perpendicular to the surface can be obtained [4].

Elastic recoil detection (ERD) is similar to RBS, but

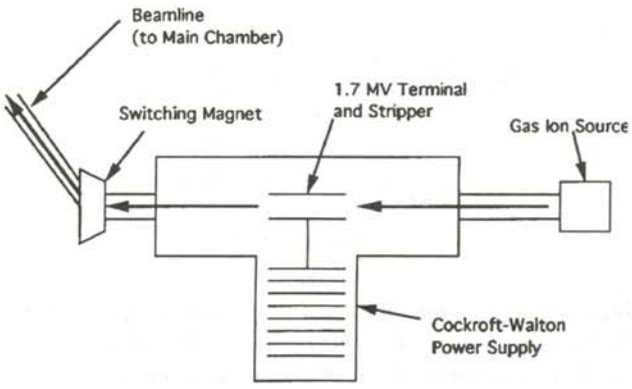

Figure 2

Simplified diagram of the Cockroft-Walton tandem accelerator.

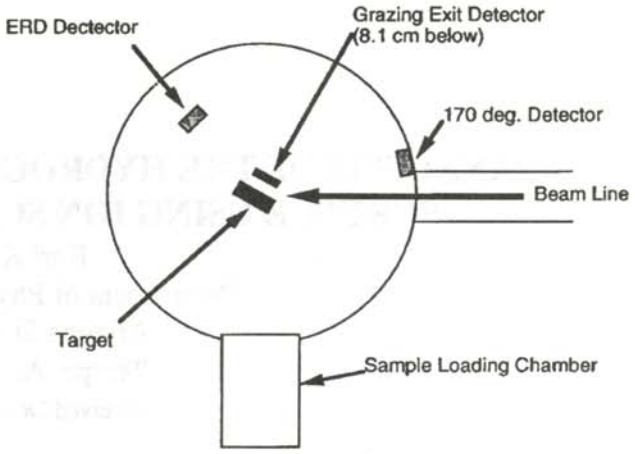

Figure 3

High vacuum main chamber used in the scattering experiments. The grazing exit detector is located 8.1 cm below the plane defined by the beamline, the 170 degree detector and the ERD detector.

makes use of forward recoiled atoms. Thus, it is useful for depth profiling of light elements such as hydrogen which cannot be used as targets in backscattering. [5]

EXPERIMENTAL TECHNIQUE

The incident ions used in this experiment were produced in a duoplasmatron gas ion source, first with a negative charge. They were injected into a Cockroft-Walton tandem accelerator where they were accelerated towards a +1.7 MV terminal. Near the terminal, the negative ions were stripped of electrons, making them positively charged. Then the ions were accelerated away from the positive high-voltage terminal towards a switching magnet, which selected the desired ion species. The ions passed through a collimating beam line into the main chamber. The accelerator setup is shown in Figure 2.

The scattering experiments were performed in a high-vacuum chamber, evacuated with an ion pump to a pressure of about 10^{-6} Pa. The sample was loaded into the chamber through a secondary chamber called a load lock, which was baked to remove hydrocarbons from the chamber walls. The load lock was pumped from atmosphere to 10 Pa with a cryogenic sorption pump system. A turbomolecular pump further reduced the load lock pressure to about 10^{-4} Pa. After about 5 minutes of pumping, the sample was transferred to the main chamber.

Three solid state surface barrier detectors, which are insensitive to charge state, were used in the main chamber. One was used as a forward scattering detector, the second as a 170° backscattering detector. Both were centered on the same horizontal plane as the incident beam and the sample. The third detector was placed 8.1 cm below the sample and used as a grazing exit detector to enhance the energy and depth resolution. [3] The high-vacuum chamber is shown in Figure 3.

The grazing exit detector was covered with a narrow slit which was parallel to the vertical plane of the sample. The scattering angle of particles detected at each end of the slit was different. For example, if the incident beam is aligned with the [001] axis, there is a 54.75 angle between the beam line and the sample normal. This results in a scattering angle of 108.7° for particle detected at one end of the slit and 107.1° for particles detected at the other end of the slit. This gives an angular spread of about 1.6 ° and a kinematic spread of 5 keV for 1 MeV He+ particles. This is less than the 14 keV intrinsic energy resolution of the detector, sharpening the energy resolution of our detection system.

After preparation, the sample was placed in the high vacuum target chamber. ERD was performed on the sample to determine the amount of hydrogen coverage. A sample of 400 nm thick polystyrene (CH) on a silicon substrate was used as a reference A 2.8 MeV He++ ion beam was directed at an angle of 75° with respect to the sample normal. The forward detector was placed at a scattering angle of 30°. A mylar filter was placed in front of the detector to limit the detected particles to hydrogen.

An incident beam of 1.0 MeV He+ ions was used to probe the sample. The [001] crystal axis was found at 54.75° from the normal [111] axis. A channeling spectrum was obtained for this orientation for both the 170° detector and the grazing exit angle detector. A bismuth-implanted silicon sample was used as a calibration standard [7] and was placed in the vacuum chamber with the same geometry as the sample under investigation. The surface peak intensity (Nt_{SP}) was calculated using Equation 1 by

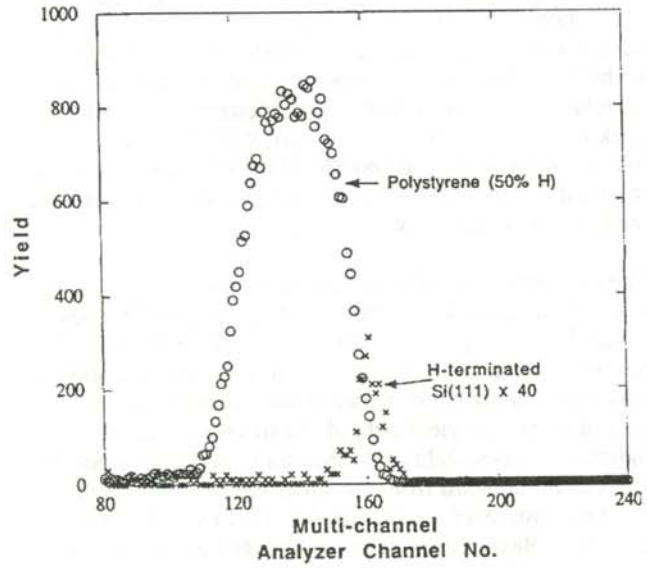

Figure 4

ERD spectra of hydrogen for the hydrogen-terminated Si(111) surface (x) and for the 400 nm thick polystyrene standard (o). The hydrogen-terminated Si(111) spectrum is shown at 40 times the actual size.

comparing the area of the surface peak (A_{SP} - shown as Area 1 in Figure 1) to the area of the Bi peak (A_{Bi}) found from a backscattering spectrum of the calibration standard.

$$Nt_{SP} = \frac{A_{SP}}{A_{Bi}} \cdot \frac{A_{Bi}^2}{A_{Si}^2} \cdot \frac{Q_{Bi}}{Q_{Si}} \cdot \frac{1}{\cos(\theta_o)} \cdot Nt_{Bi} \qquad (1)$$

The areal density of the bismuth standard (Nt_{Bi}) had been measured at 4.77×10^{15} atoms/cm^2 .[7] The ratio of the total incident charge delivered by the incident beam in each experiment (Q_{Bi}/Q_{SP}) was measured by a charge digitizer and counter. θ_o is the angle between the incident ion beam and the sample normal. Corrections were made for the transformation of the scattering cross sections from the center-of-mass reference frame to the laboratory reference frame. These corrections are only ≈0.2%.

An angular scan was performed about the [001] axis. A computer-interfaced goniometer stepped θ_o in 0.05° increments. Spectra such as the one shown in Figure 1 were obtained simultaneously from the 170° detector and the grazing exit angle detector.

Sample Preparation

To produce a uniform, flat, hydrogen-terminated silicon [111] surface, the sample was prepared using cleaning and etching techniques performed inside a laminar flow hood in a Class 100 clean room. Prior to etching, the sample and related handling equipment were cleaned for 10 minutes at 80 °C using a 4:1:1 solution of deionized H_2O, H_2O_2 and NH_4OH. The oxide layer on the sample was removed with the application of a 40% solution of HF at room temperature for one minute. The hydrogenated flat surface was obtained with an etch at room temperature for 6 minutes with NH_4F_2 .[1,6]

STM studies have shown this surface to be essentially flat on the atomic scale, uniformly hydrogen-terminated and stable against reactions in the atmosphere except with hydrocarbons.[1,2] Visual inspection of the sample during the cleaning and etching process gave immediate qualitative verification of how well the surface was being cleaned and etched. The appearance of bubbles on the sample surface during immersion in NH_4F_2 indicated a large amount of etching activity. This occurred for surfaces with a high density of steps and terraces. In contrast, a "good" surface was one that was relatively flat due to a sharp interface in a previously grown oxide layer. Such a surface showed almost no activity during NH_4F_2 immersion.

RESULTS AND ANALYSIS

ERD was performed on the hydrogen-terminated silicon surface and the reference polystyrene using 2.8 MeV He++ ions. The RUMP computer program [8] was calibrated by running a simulation to match the polystyrene spectrum. Figure 4 shows the ERD results for the 400 nm polystyrene standard and the hydrogen-terminated Si(111)

surface. The dramatic difference between the standard with about 50% hydrogen and a silicon surface with a thin layer of hydrogen on the surface can bee seen. Further work must be done to quantitatively obtain the areal density of hydrogen on the surface.

Channeling spectra were obtained from both backscattering detectors for samples which showed both large and small amounts of activity during the cleaning and etching process. Surface peak intensities were determined using Equation 1. For the surface which showed a large amount of activity during the cleaning and etching process, a surface peak intensity of 5.1±0.3 atoms/row was obtained using the 170° detector and 7.4±0.5 atoms/row for the grazing exit geometry. Because the data were taken simultaneously for the two detector, the numbers should overlap within their experimental data. It is uncertain why this is not the case.

In contrast, the surface which was characterized as "good" because of low surface activity during the etching, had a surface peak intensity of 3.0±0.2 atoms/row for the grazing exit geometry and 3.6±0.2 atoms/row for the 170° geometry. The size of these atoms/row values suggest very little displacement perpendicular to the sample [4] and also demonstrates the importance of sample preparation. While these numbers are very similar, they should overlap within their uncertainties.

The surface peak measurements have statistical uncertainties, there are background uncertainties and errors associated with the bismuth standard. Systematic errors associated with the measured areal density of the standard were ≈2% [7] The superior energy resolution of the grazing exit angle geometry resulted in a lower background subtraction

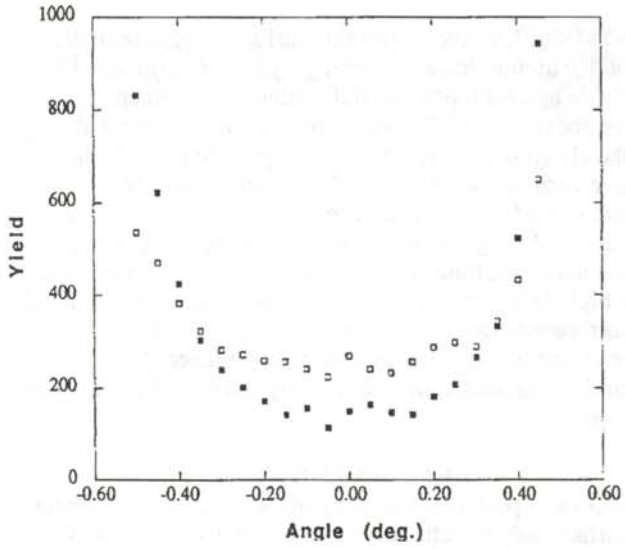

Figure 5

Angular scan using grazing exit angle geometry for low etching activity sample. Open squares represent Area 1 and closed squares represent Area 2.

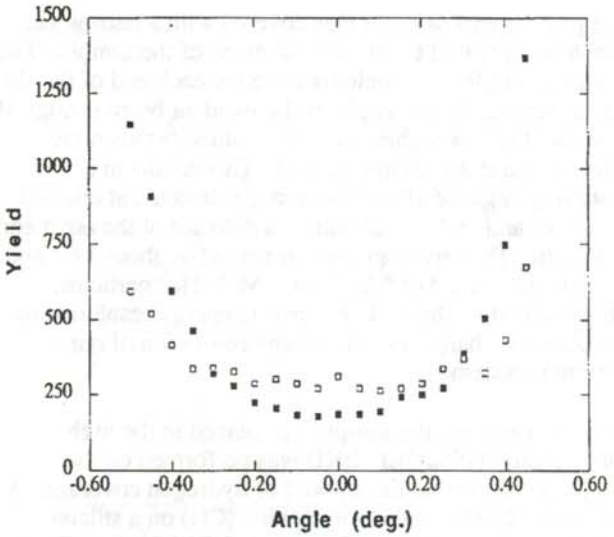

Figure 6

Angular scan using 170° geometry for low etching activity sample. Open squares represent Area 1 and closed squares represent Area 2.

and less uncertainty in the surface peak intensity. The uncertainty attributed to the background subtraction of 5% for the 170° geometry and 4% for the grazing exit angle geometry. The statistical uncertainties associated with the surface peak calculations were generally ≈2% for the surface peak area (A_{SP}) and less than 1% for the bismuth standard calibration area (A_{Bi}). The total uncertainty in the surface peak was ≈6%.

The surface peak intensities can be compared to computer simulations for bulk like surface structures. Simulations have been performed for such surfaces both with and without consideration for atomic vibrations and two-atom correlations. [4] An experimentally determined surface peak intensity of 4.6 ± 0.2 atoms/row for the [001] direction of a reconstructed Si(111)-(7x7) surface has been reported. [4] This value indicated large displacements in at least two monolayers of > 0.04 nm. [4]

The data for the angular scans around the [001] axis for the low-activity sample are shown in Figures 5 and 6. Because the areas chosen for plotting are arbitrary, only the relative angular positions are important. The data show no appreciable asymmetry between the surface peak and the area of minimum yield behind the surface peak. This indicates the possibility that the atoms in one monolayer are relaxed outward from the surface while the atoms in another monolayer are contracted. However, if one or more monolayers were displaced inward or outward, the surface peak intensity for the [001] aligned geometry would be much larger. [4] Another more probable possibility is that no major displacements occur perpendicular to the surface.

SUMMARY

The remarkably flat, well passivated and uniformly hydrogen-terminated Si(111)-(1x1) surface has been studied using ion channeling and elastic recoil detection techniques. The data obtained suggest that very little relaxation or contraction of surface or near surface atoms occurs perpendicular to the sample surface. However, the data obtained depend critically on the quality of the sample surface after the cleaning and etching process.

ACKNOWLEDGMENTS

The author thanks Robert J. Culbertson for his guidance in this work and Roger Garcia for his support. This work was performed under the auspices of the Arizona State University Physics Research Experience for Undergraduates Program, sponsored by the National Science Foundation and Arizona State University.

REFERENCES

* Present address of author: Physics Department, Gustavus Adolphus College, St. Peter, MN, 56560

1. G.S. Higashi, R.S. Becker, Y.J. Chabal and A.J. Becker, Appl. Phys. Lett., 58, (1991), p. 1656.
2. Y.J Chabal, J. Mole. Struct., 292, (1993), p. 65.
3. W.K. Chu, J.W. Mayer and M.A. Nicolet, Backscattering Spectrometry, Academic Press, New York, (1978).
4. R.J. Culbertson, Phys. Rev. Lett., 45, (1980), p. 2043.
5. B.L. Doyle and D.K. Brince, Nucl. Instrum. and Methods., B35, (1988), p. 301.
6. Y.J. Chabal, private communication.
7. J. L'Ecuyer, J.A. Davies and N. Matsunami, Nucl. Instrum. and Methods, 160, (1978), p. 337.
8. L.R. Dolittle, Nucl. Instrum. and Methods, B9, (1985) p. 334.

FACULTY SPONSOR

Dr. Robert J. Culbertson
Department of Physics and Astronomy
Arizona State University
Tempe, AZ 85287-1504

The Journal of Undergraduate Research in Physics

The Journal of Undergraduate Research in Physics is the journal of Sigma Pi Sigma and the Society of Physics Students. It is published by the Physics Department of Guilford College, Greensboro NC 27410. Inquiries about the journal should be sent to the editorial office.

The Journal of Undergraduate Research in Physics

Editorial Office -
The Journal of Undergraduate Research in Physics
Physics Department
Guilford College
Greensboro, NC 27410
910-316-2279 (voice)
910-316-2951 (FAX)

Editor -
Dr. Rexford E. Adelberger
Professor of Physics
Physics Department
Guilford College
Greensboro, NC 27410
ADELBERGERRE@RASCAL.GUILFORD.EDU

The Society of Physics Students

National Office -
Dr. John Rigden, Acting Director
Ms. Sonja Lopez, SPS Supervisor
Society of Physics Students
American Institute of Physics
1 Physics Ellipse
College Park, MD 20740
301-209-3007

President of the Society -
Dr. Fred Domann
Department of Physics
University of Wisconsin at Platteville

President of Sigma Pi Sigma -
Dr. Jean Krisch
Department of Physics
University of Michigan, Ann Arbor